

VARIATION IN THE SCATTERING SHROUD SURROUNDING MARKARIAN 231^{1,2}

S. C. GALLAGHER,³ GARY D. SCHMIDT,⁴ PAUL S. SMITH,⁴ W. N. BRANDT,⁵ G. CHARTAS,⁵
SHAVONNE HYLTON,⁶ D. C. HINES,⁷ AND M. S. BROTHERTON⁸

To Appear in The Astrophysical Journal

ABSTRACT

We present a detailed study of the nuclear structure of the highly polarized broad absorption line quasar, Mrk 231, through a multiwavelength campaign of *Chandra* observations, optical spectroscopy, optical spectropolarimetry, and imaging polarimetry. This campaign was designed to extend the 40 ks *Chandra* study of Gallagher et al. and the optical and UV spectropolarimetric study of Smith et al. to probe variability on multiple timescales. As direct emission from the nucleus is heavily obscured at optical through X-ray wavelengths, the detailed study of scattered emission has led to insights into the stratified and complex central region of this active galaxy. Though significant continuum variability is not detected in any of the three new 40 ks *Chandra* observations, we investigate Fe K α emission features in the individual and combined spectra. Comparing echelle spectra of the Na I D absorption lines with the literature, we show that one system disappeared in 2000 only to reappear in later epochs. Notably, we detect a large decrease in polarization across the entire optical spectrum of Mrk 231 from 1995 to 2003. Though the polarization fraction fell, e.g., from 4% to 3% at $\lambda_{\text{obs}} \sim 6000\text{\AA}$, the polarization position angle spectrum remained unchanged. The optical polarization behavior is consistent with a decrease in the flux scattered by circumnuclear material on spatial scales where the broad-line region is resolved by the scattering material. Ultraviolet imaging polarimetry of Mrk 231 by the *Hubble Space Telescope* sets an upper limit on the distance between the active nucleus and the scattering regions of <20 pc.

Subject headings: galaxies: individual (Markarian 231) — galaxies: nuclei — galaxies: Seyfert — polarization — ultraviolet: galaxies — X-rays: galaxies — quasars: absorption lines

1. INTRODUCTION

The variability of emission from active galactic nuclei (AGNs) has long been employed in efforts to discern the structure and physics of material near the central energy source. The dramatic changes in brightness and polarization of the continua of radio-loud objects, particularly at short wavelengths, played an important role in developing the popular model of a relativistically beamed jet emitting by the synchrotron mechanism (e.g., Blandford & Rees 1978). The effects of more isotropic changes in luminosity have been exploited by the “reverberation mapping” technique to infer the size, thick-

ness, and ionization properties of the broad emission-line region, and more recently to identify systematic trends in nuclear parameters between various classes of AGNs (e.g., Netzer & Peterson 1997).

Evidence for changes of the *structure* of the nuclei of active galaxies can be found in the appearance and disappearance of shoulders and other features in the profiles of broad emission lines, modifications of the Balmer decrements, and in certain cases in the replacement of a normally centrally peaked profile by one that is strongly double-peaked (Ulrich et al. 1997 and references therein). Some of these effects appear to be induced by luminosity changes of the central continuum source, but others require mass motions or the redirection of an illuminating beam, also known as the ‘searchlight’ effect. At larger radii, variations in the properties of absorbing gas as indicated by changes in UV absorption lines have been detected on timescales of ~ 1 yr in several Seyfert galaxies, with explanations including both luminosity-induced ionization changes and the motion of absorbers across our line of sight (e.g., Gabel et al. 2003 and references therein). Similarly, large column density variations have been observed in X-ray studies of absorbed AGNs on timescales of months to years (e.g., Risaliti et al. 2002; Gallagher et al. 2004).

The luminous Type 1 (broad emission line) AGN Markarian 231 is well known to exhibit no less than three displaced optical absorption-line systems in Na I, He I, and Ca II (Boksenberg et al. 1977), and a fourth appeared in observations made in 1988 (Boroson et al. 1991). Further variability in the strengths of the absorption lines has been reported in subsequent years

¹ Some of the data presented here were obtained with the MMT Observatory, a facility operated jointly by The University of Arizona and the Smithsonian Institution.

² Based on observations obtained with the Upgraded Fiber Optic Echelle Spectrograph on the Hobby-Eberly Telescope, which is operated by McDonald Observatory on behalf of the University of Texas at Austin, the Pennsylvania State University, Stanford University, the Ludwig-Maximilians-Universität, Munich, and the George-August-Universität, Göttingen.

³ Department of Physics & Astronomy, University of California – Los Angeles, Mail Code 154705, 475 Portola Plaza, Los Angeles CA, 90095-4705, sgall@astro.ucla.edu

⁴ Steward Observatory, The University of Arizona, Tucson AZ 85721; gschmidt@as.arizona.edu, psmith@as.arizona.edu

⁵ Department of Astronomy & Astrophysics, The Pennsylvania State University, University Park, PA 16802; niel@astro.psu.edu, chartas@astro.psu.edu

⁶ Center for Space Research, Massachusetts Institute of Technology, 77 Massachusetts Avenue, Cambridge, MA 02139

⁷ Space Science Institute, 4750 Walnut Street, Suite 205, Boulder, CO 80301; dean.hines@colorado.edu

⁸ Department of Physics & Astronomy, University of Wyoming, Dept. 3905, Laramie, WY 82071; mbrother@uwyo.edu

(Kollatschny et al. 1992; Forster et al. 1995, hereafter FRM) and Mg II λ 2800 absorption associated with one of the systems reported by Smith et al. (1995, hereafter SSAA). This observation, coupled with the source’s high intrinsic luminosity, qualified Mrk 231 as a low-ionization broad absorption-line (LoBAL) quasar. LoBAL quasars are notoriously weak X-ray emitters (Green et al. 2001; Gallagher et al. 2002a); therefore the proximity ($z = 0.0422$) of Mrk 231 makes it by far the most easily studied example of this class in X-rays.

The fact that most of the $\sim 4 \times 10^{12} L_{\odot}$ luminosity of Mrk 231 appears in the infrared (Rieke & Low 1972) was early evidence that the central energy source is heavily obscured along most sightlines. This is strongly supported by the paucity of emission from the narrow-line region (specifically, the absence of [O III] flux; Hamilton & Keel 1987), and the shape and luminosity of the 2–10 keV X-ray spectrum imply that the nucleus is only seen via reflection and/or scattering in that band (Maloney & Reynolds 2000; Gallagher et al. 2002b, hereafter G02). An analysis of 15–60 keV *Beppo-SAX* Phoswich Detector System (PDS) data by Braitto et al. (2004) confirmed this interpretation with the detection, for the first time, of the direct X-ray continuum absorbed by an intrinsic column density of $N_{\text{H}} \sim 2 \times 10^{24} \text{ cm}^{-2}$. Absorption of this magnitude completely blocks the direct 2–10 keV continuum, which has an absorption-corrected luminosity $L_{2-10} \sim 10^{44} \text{ ergs s}^{-1}$ (Braitto et al. 2004). The observed, nonthermal 2–8 keV continuum, with $L_{\text{X}} \sim 2 \times 10^{42} \text{ ergs s}^{-1}$, must therefore be reprocessed emission. However, the 2–8 keV flux variability on timescales of hours detected by G02 with *Chandra* indicates that the X-ray scattering medium is compact, with spatial scale of $\sim 10^{15} \text{ cm}$. Given the proximity of this gas to the central continuum source, this scattering medium is likely to be highly ionized. Obscuration and the attendant scattering of nuclear light by pervasive dust clouds at much larger radii, $R \gtrsim 1 \text{ pc}$, give rise to polarization of the optical-UV light, and polarization fractions that reach 15% in the near-UV have made the object a popular target for polarimetric studies with increasing quality over the past two decades (Thompson et al. 1980; Schmidt & Miller 1985; Goodrich & Miller 1994; SSAA; Smith et al. 2004).

The sensitivity of both the X-ray spectrum and the optical polarization of Mrk 231 to the geometry of scattering on different physical scales, and the insight that variations in these diagnostics might lend to our knowledge of the structure of the nuclear regions of a luminous Type 1 AGN, have led us to carry out a program of high-quality, ground-based optical spectropolarimetry and 0.5–8 keV spectroscopy with the *Chandra* X-ray Observatory (Weisskopf et al. 2002). In this paper we present the results of that study as well as optical echelle spectroscopy and UV polarimetry from different epochs that contribute additional information on the properties of the nucleus.

The cosmology assumed throughout has $H_0 = 70 \text{ km s}^{-1} \text{ Mpc}^{-1}$, $\Omega_{\text{M}} = 0.3$, and $\Omega_{\Lambda} = 0.7$. For Mrk 231 at $z = 0.0422$, 1 arcsecond corresponds to a physical scale of 833 pc.

2. X-RAY OBSERVATIONS AND ANALYSIS

Mrk 231 has been observed 4 times with *Chandra*, each time at the aimpoint of the ACIS (Garmire et al. 2003) back-illuminated S3 detector. The first observation of 2000 Oct 19 (observation 1031) was in full-frame mode. The subsequent three observations of 2003 Feb (observations 4028–30) were performed in 1/2 subarray mode in order to reduce the $\sim 7\%$ pile-up fraction of the first observation (G02). Each ACIS observation was between 36–39 ks long; Table 1 presents the log of the observations, including dates, exposure times, and soft and hard-band count rates. The Δt of ~ 1 week between observations 4028, 4029, and 4030 was chosen to probe times with a scale intermediate between the hours and years time scales of previous observations. Physically, this corresponds to structure on scales of $\sim 10^{16} \text{ cm}$, the scale of the thick, highly ionized gas postulated by Murray et al. (1995) to shield a radiatively driven BAL wind from becoming overionized by the ionizing X-ray continuum.

The *Chandra* data were processed with the standard *Chandra* X-ray Center (CXC) pipeline from which the level 1 events file was used. The data were filtered on good time intervals. The standard pipeline processing introduces a 0.5 software randomization into the event positions, which degrades the spatial resolution by $\sim 12\%$ (Chartas et al. 2002). This randomization is done to avoid aliasing effects noticeable in observations with exposure times of less than 2 ks. Since spatial resolution was important for our analysis and the ACIS observations were significantly longer than 2 ks, we removed this randomization from the ACIS observation by recalculating the event positions in sky coordinates using the CIAO tool, *acis_process_events*. The ACIS-S3 imaging data were corrected for radiation damage sustained by the CCDs during the early months of *Chandra* operations using the software described in Townsley et al. (2002). This procedure mitigates the effects of charge transfer inefficiency (CTI) that introduces positional dependence of the gain, quantum efficiency, and grade distribution. CTI-corrected ACIS-S3 data allow a single redistribution matrix file (rmf) to be used across the whole CCD. After CTI-correction, the data were filtered to keep “good” time intervals and *ASCA* grades (grades 0, 2, 3, 4, and 6). Filtering on “status” can remove X-ray events from the nucleus because X-rays can be inappropriately tagged as cosmic-ray afterglows. Therefore, the values in the status column for cosmic-ray afterglows were ignored for the final filter on “good” status.

2.1. Variability Analysis

Given the significant hard-band X-ray variability detected in the first *Chandra* observation, we first searched for count-rate changes both within and between the observations. The time and energy of each event within a 3''-radius source circle centered on the peak of the X-ray emission were extracted from the reduced events file for each observation. The unbinned full (0.5–8.0 keV), soft (0.5–2.0 keV), medium (2.0–5.0 keV), hard (2.0–8.0 keV), and very hard (5.0–8.0 keV) band event arrival times for each observation were evaluated with the non-parametric Kolmogorov-Smirnov test to search for variability within each observation. For the new observations, no significant variability was detected in any band. The original

data from 2000 (observation 1031) were downloaded from the public archive, rereduced with CIAO 3.0 as outlined above, and retested. As presented in G02, we recovered significant variability in the medium and hard bands at the $> 99\%$ confidence level; this result was also confirmed by the independent analysis of Ptak et al. (2003).

To check for variability between observations, the background-subtracted nuclear count rates were compared in the five bands. The chosen background region was a source-free annulus with an inner radius of $40''$ and an outer radius of $50''$, well outside of the galaxy, centered on the nucleus. Figure 1 presents these data. The full-band count rate is remarkably stable, but there appears to be a slight shift over the course of observations, with more hard-band counts relative to soft-band counts in the last observation than in the preceding ones. This trend is slight however, and we investigate any possible spectral hardening further with spectral analysis.

2.2. Nuclear Spectroscopy

The nuclear spectra were extracted from each reduced *Chandra* dataset independently. The source and background regions were the same as those used in the variability analysis. The auxiliary response files (arfs) and rmfs were generated with the CIAO 3.0 tools *mkarf* and *mkrmf*, respectively.

The final, preferred model from G02 for the fit to the *Chandra* spectrum included a thermal component from the nuclear starburst as well as three absorbed power-law components with different normalizations and intrinsic column densities (see Figure 9d of G02). Given the observed 2–8 keV luminosity of the source (~ 100 times fainter than expected based on both the dereddened UV luminosity and the > 10 keV X-ray spectrum) and the known complexity of the scattering geometry derived from optical polarization studies (SSAA), these power-law continua were interpreted as direct continuum X-rays scattered into the line of sight by distinct structures, and therefore passing through different amounts of absorption. The scattering was inferred to be by electrons in highly ionized plasma, thus preserving the shape of the intrinsic spectrum. In G02, the photon index of each power-law model was fixed to $\Gamma = 2.1$, based on the correlation of $H\beta$ FWHM and Γ found by Reeves & Turner (2000) from *ASCA* spectral fitting of quasars. To evaluate this model in the context of the new *Chandra* data, we examined the combined, average spectrum from the three new observations to increase the signal-to-noise ratio. With these data, the power-law photon index can be fit independently. We do not incorporate the data from the first *Chandra* epoch because they were mildly piled-up and taken in a different mode (full array rather than $1/2$ subarray).

To create an average nuclear spectrum, the three unbinned spectra and background spectra were each added together using the FTOOL *mathpha*. An average arf and rmf were created by weighting by the 0.5–8.0 keV counts using *addarf* and *addrmf*, respectively. The combined spectrum (with a total exposure of 114.3 ks and 4300 counts) was then fit using the X-ray spectral-fitting tool, XSPEC (Arnaud 1996). Three absorbed power-law models plus a Raymond-Smith plasma were applied to the combined spectrum; Γ was tied for each power law. An acceptable fit ($\chi^2/\nu = 174.8/153$) was

found for this model with $\Gamma = 1.92^{+0.37}_{-0.70}$. However, given the relatively featureless spectrum, this solution is not unique, and much lower values of Γ also provide statistically acceptable fits. As $\Gamma \sim 1.9$ is typical of radio-quiet quasars and more plausible in the context of this model, we fixed $\Gamma = 1.92$ to determine the errors in the remaining parameters. The column densities (assumed to be neutral) for the three power laws are $N_{\text{H}} = (0.19^{+0.04}_{-0.03}, 4.6^{+0.92}_{-0.55}, 45^{+17}_{-10}) \times 10^{22} \text{ cm}^{-2}$, similar to the values listed in Table 2 of G02. This model does not include a component corresponding to the highly absorbed ($N_{\text{H}} \sim 2 \times 10^{24} \text{ cm}^{-2}$) direct X-ray continuum studied by Braito et al. (2004) because this component does not contribute significant counts to the *Chandra* spectrum. The best-fitting temperature for the Raymond-Smith plasma is $kT = 0.89^{+0.05}_{-0.03}$ keV. Though the spectral bump near 1 keV (likely from spectrally unresolved Fe L emission lines) is fit by this model, it is also possible that there is a contribution from photoionized plasma, and Turner & Kraemer (2003, hereafter TK) suggested that an emission feature seen at ~ 0.45 keV in the *XMM-Newton* spectrum might be a C IV radiative recombination line.

TK detected a broad, Fe K α emission line with an equivalent width $EW \sim 450$ eV, a rest-frame energy $E = 6.49 \pm 0.12$ keV, and $\sigma = 0.17 \pm 0.12$ keV in the 17.3 ks *XMM-Newton* EPIC-pn spectrum of Mrk 231. Such a strong, broad feature is not evident in this 0.5–8.0 keV combined spectrum, and adding a broad line does not make a significant improvement in the spectral fit ($\Delta\chi^2 = -2.8$ for three fewer degrees of freedom). Adding a single, unresolved line in the Fe region has a best-fitting energy of $6.64^{+0.05}_{-0.09}$ keV and gives $\Delta\chi^2 = -5.5$ for two fewer degrees of freedom.

To focus further on the nuclear spectrum in general and the Fe K α region in particular, we follow the example of TK by ignoring the data below 3.0 keV where starburst emission is significant and fitting the 3.0–8.0 keV counts with a single power-law model for the continuum. From G02, this is also the region of the spectrum that showed significant variability in observation 1031 of 2000 Oct. To account for the Fe K α edge absorption expected from multiple absorbers (not otherwise included in this model), we also add an edge with the rest-frame energy fixed at 7.12 keV, the ionization energy of neutral Fe. This two component model is sufficient to fit the data, with $\chi^2/\nu = 69.0/69$, and adding a broad line does not significantly improve the fit ($\Delta\chi^2 = -3.2$ for three fewer degrees of freedom). Convolution of the best-fitting *XMM-Newton* model with the *Chandra* response and allowing Γ , the continuum normalization, and τ_{max} (the maximum optical depth of the ionization edge) to vary while keeping the Fe K α line parameters fixed does not provide a better fit ($\chi^2/\nu = 72.8/69$) than the power-law plus edge model alone. Freeing the continuum parameters is necessary to account for both cross-calibration uncertainties and potential source variability. A strong negative residual at rest-frame ~ 6.45 keV (approximately the peak energy of the *XMM-Newton*-detected emission line) suggests that *Chandra* is resolving the broad line seen by TK into two narrow lines. At 6 keV, the *XMM-Newton* EPIC-pn has an effective area about 4 times larger than

that of ACIS-S3.⁹ Our 114 ks observation is about 6.6 times longer than the *XMM-Newton* observation, and therefore the *Chandra* data have better photon statistics. Both the *Chandra* and *XMM-Newton* data can be successfully fit with two unresolved ($\sigma = 0.01$ keV) gaussian lines, with consistent line energies of ~ 6.3 and ~ 6.6 keV. In the *XMM-Newton* data, with fewer counts in the observed-frame 5.8–6.7 keV band (~ 140 versus ~ 210 for the combined *Chandra* spectrum), two gaussians are not preferred over a single, broad gaussian. Figure 2 shows the combined data and preferred spectral model, and the parameters from the preferred spectral models for both the *Chandra* and *XMM-Newton* data are presented in Table 2.

From visual inspection of a merged 5.8–6.7 keV (rest-frame 6–7 keV) image, a $3''$ -radius source cell encompasses all of the counts in this band. That is, there is no evidence from the *Chandra* data of significant Fe-band emission coming from the host galaxy. Therefore, any discrepancies between the observation presented in TK and the *Chandra* data do not arise from the different beam sizes of *Chandra* and *XMM-Newton*.

We investigate further the possibility of nuclear spectral variability between the 5 observations (four *Chandra* and one *XMM-Newton*). Again, each spectrum was initially fit jointly with a power law model and an absorption edge fixed to 7.12 keV. Both Γ and τ_{\max} were tied for the fit, and the power-law normalizations were free to vary for each observation. To look for iron emission, the data in the iron band (rest-frame 6–7 keV, observed-frame 5.8–6.7 keV) were ignored for this continuum fit. The *Chandra* residuals from this joint-spectral fitting are shown in Figure 3. For the final observation, there is no strong evidence of iron emission. For the first observation, a series of positive residuals in the iron band is suggestive of a broad emission feature, as found by TK. In addition, for the middle two observations, Feb 03 and Feb 11, there are consecutive positive residuals at the $1-2\sigma$ level in the iron-band region. To examine these features more closely, we fit the spectra individually.

For each observation, the power-law model with an edge at 7.12 keV was applied to the data. The values of Γ , τ_{\max} , and the power-law normalization were free to vary. In each case, the fit was acceptable with $\chi^2/\nu=29.8/30$, $29.1/31$, $30.3/33$, and $13.1/31$ for observations 1031, and 4028–30, respectively. Next, a narrow iron line was added to each model as a redshifted gaussian with the energy free to vary between rest-frame 6–7 keV. The value for σ was fixed to 0.01 keV, unresolved at ACIS CCD resolution. In chronological order, the new values for χ^2 were 26.8, 22.4, 21.7, and 13.1 for two fewer degrees of freedom. Of these, only the middle two (observations 4028 and 4029) indicate a significant improvement in the model fit with $\Delta\chi^2 = -6.7$ and -8.6 , respectively. According to the *F*-test, the addition of the gaussian component improved the individual models at the $> 97\%$ and $> 99\%$ confidence level for the data from observation 4028 and 4029, respectively. For observation 1031, a broad line with σ free to vary was also tested. For three fewer degrees of freedom from the power-law plus edge model, $\Delta\chi^2 = -6.6$, indicating an improvement at the $\sim 92\%$ level over the continuum model alone. Formally,

these confidence levels should be lower, as they apply to a single observation (rather than the four we are presenting), but they are still useful as a relative gauge of the improvement. The values and errors for the parameters of the preferred model for each spectrum are listed in Table 2.

In Figure 4, the contour plots for the line flux versus line energy for 4028 and 4029, the observations with two possible narrow lines, are plotted. As is evident from the figure, the 68% and 90% contours do not overlap; the energies are not consistent. The fluxes and EWs found for both observations are however consistent.

2.3. X-ray Properties of the Galaxy

A merged event file of the three new observations was created using the CIAO script *merge_all*. This script reprojects the positions of events from all images into a common frame so that they can be combined. The images were then adaptively smoothed using the CIAO tool *csmooth*. The X-ray emission from the galaxy based on the 40 ks 1031 observation was described in detail by G02, and so we only comment briefly on the new information obtained from these additional data.

From the full-band image (Figure 5), the deeper data allow us to see ring structure around the nucleus. A radial surface-brightness profile of the soft-band (0.35–2.0 keV) counts centered on the nucleus (Figure 6) reveals an enhancement of the X-ray emission at $R \approx 2''.6$. This radius is approximately halfway between the two bright optical ‘shells’, S1 and S2 (as labeled by Lípari et al. 2005), seen in *HST* images. The overall galactic emission is structured and asymmetric, with X-ray enhancements to the northeast and a deficit to the west of the nucleus; both were previously seen in the 1031 image. The northeast structure is likely from photoionized (rather than collisionally ionized) gas as it coincides with an optically bright region attributed to [O III] emission (Hutchings & Neff 1987). In the full-band image, the off-nuclear point-source detected by G02 is no longer present, however, a second one (only evident at energies < 3 keV) has appeared to the southwest of the nucleus. The inferred variability of both sources is consistent with an identification as luminous X-ray binaries (e.g., Fabbiano et al. 2003), preferentially found in actively star-forming galaxies.

The three-color image, made by combining 0.35–1.2 (red), 1.2–3.0 (green), and 3.0–8.0 keV (blue) csmoothed images illustrates the energy dependence of these features (Figure 5). The asymmetry of the hard emission surrounding the nucleus causes the image to appear bluer to the west of the nucleus. Except for a compact region within $\sim 4''$ of the nucleus, the galaxy is not detected at energies > 3 keV.

3. OPTICAL OBSERVATIONS AND ANALYSIS

3.1. Echelle Spectroscopy

Mrk 231 was observed with the 9.2 m Hobby-Eberly Telescope (HET; Ramsey et al. 1998) at McDonald Observatory using the Upgraded Fiber Optic Echelle Spectrograph (UFOE; Harlow et al. 1996) in 2000 January and April. These observations were made to search for relatively short-time scale (weeks to months) variations in the prominent Na I D absorption systems that are

⁹ http://heasarc.gsfc.nasa.gov/docs/xmm/about_why.html

blueshifted $5000\text{--}6000\text{ km s}^{-1}$ from the systemic velocity of the host galaxy. All of the data were acquired using a $400\ \mu\text{m}$ ($2''$) fiber with sky subtraction accomplished with a second $2''$ fiber offset from the galaxy. The spectra have a resolution of $\sim 0.8\ \text{\AA}$ in the echelle order containing the Na I D absorption features. As summarized in Table 3, the 2000 January observations consisted of three 200 s exposures of the nucleus on January 6 followed by four 900 s exposures on January 13. No significant differences were seen between the two sets of observations and the results were averaged. Similarly, the 2000 April 3 dataset is an average of three 900 s exposures.

The January and April data were then inspected for differences in the positions, widths, and equivalent widths (EWs) of the various absorption systems of Na I D. The lower spectrum shown in Figure 7 is the difference spectrum (Jan – Apr) between the two epochs, after normalizing the spectra to the surrounding continuum. Again, no significant differences are seen between the two epochs, and the average of the two spectra is displayed as the upper trace in Figure 7, with individual line systems labeled according to the notation of FRM and quantified in Table 4. At the resolution and signal-to-noise ratio of the HET observations, the doublet splitting is cleanly resolved and subsystems can be recognized in both systems I and II. The D_1 component of system II is a tentative identification within the main trough of system I at about the correct position relative to D_2 . Expected positions of the lines for the system III doublet (Boroson et al. 1991) are marked, but it is clear that these features were absent in early 2000.

3.2. Ground-Based Imaging and Spectropolarimetry

Optical spectropolarimetry of Mrk 231 was obtained on several nights during 2002–2004 with the spectropolarimeter SPOL (Schmidt et al. 1992). This is the same instrument that was used for the observations published by SSAA from 1992–1993, and all acquisition, calibration, and reduction procedures are common to the two epochs. As with other dual-beam designs, the instrument achieves high throughput while accurately cancelling sky background and avoiding systematic effects to better than 1 part in 1000. Calibration of the polarizing efficiency of the optics is performed by observations of a continuum source through a fully polarizing prism each observing run. However, the use of different interstellar polarization standard stars for the various observing runs can result in a dispersion of up to 1° in the overall registration of the position angle. The detector was also upgraded twice in the interval between the epochs, providing improvements in sensitivity, focus, spectral coverage, and flat-field calibration. The significant changes for polarimetry are an enhancement of the signal-to-noise ratio for a given exposure time and an improvement in spectral resolution. As summarized in the observation log in Table 3, virtually all data from the two epochs were gathered at the 2.3 m Bok telescope of Steward Observatory using a low-resolution grating ($\Delta\lambda \sim 17\text{\AA}$) with wide spectral coverage, though one dataset in each epoch utilized a $1200\ \text{line mm}^{-1}$ grating with a resolution of $8\ \text{\AA}$ to record better the polarization profiles of the $H\alpha$ emission and Na I D absorption features. In addition, observations were made at the MMT in 2004 April to investigate the diluting effects of the

host galaxy, which spans $> 1'$ (Hamilton & Keel 1987). Unfortunately, the utility of these data was compromised by poor ($\sim 2''$ FWHM) seeing at the time.

We have intercompared the polarimetric results among the individual runs of 2002–2004 in both detail and for broad wavelength intervals such as those listed in Table 3. While the effects of variable host galaxy dilution cause polarization changes at the level of $\Delta P = 0.1 - 0.2\%$ (cf. the results for the two widely different aperture sizes from consecutive nights in 2003 Feb), we find no significant variability that can be attributed to the AGN during the 16 month period. A reinspection of the data from 1992–1993 leads to the same conclusion for that period. However, there is compelling evidence for a decline of $\sim 30\%$ ($\Delta P = 1 - 2\%$ across the bandpass) in the degree of polarization during the decade that separates the two epochs. At the same time, the position angle remained constant. Means for the $\lambda\lambda 6100 - 6600$ continuum interval are $P = 3.41\% \pm 0.04\%$ at $\theta = 96^\circ 9 \pm 0^\circ 4$ for the 1990's versus $P = 2.52\% \pm 0.10\%$ at $\theta = 97^\circ 8 \pm 0^\circ 7$ for the 2000's, where the uncertainties are estimated from the scatter (rms) of the individual measurements for each epoch. The difference is easily seen in the mean polarization spectra for the two periods compared in Figure 8, and in the binned continuum values listed in Table 3. The spectropolarimetric observations were obtained under a variety of conditions and the emphasis was not on accurate absolute flux calibration, but based on the general consistency in flux level between the two epochs, any systematic change in total brightness can be limited to $\lesssim 15\%$.

Despite the change in fractional polarization level, the essential polarimetric characteristics of Mrk 231 persist between the decades. These include a slow rotation in position angle θ over the spectrum, significant changes in θ between the Fe II and Balmer lines versus the continuum, a polarized flux spectrum $P \times F_\lambda$ that is bluer than the total flux spectrum ($P_\lambda \propto \lambda^{-2}$), and emission-line features that are much narrower in polarized versus total flux.

In the interval between the two spectropolarimetric epochs, broad-band imaging polarimetry of Mrk 231 was obtained at optical and near-UV ($\S 3.3$) wavelengths. Ground-based B and R observations were made at the Bok 2.3 m telescope in late 1996 with SPOL in its imaging mode (a plane mirror is inserted behind the Wollaston prism instead of the diffraction grating), and the results are summarized in Table 3. The scale of the SPOL images is $0''.52\ \text{pixel}^{-1}$. The entries for P and θ in Table 3 are for a $3'' \times 10''$ aperture centered on the nucleus in the $51'' \times 51''$ images. This rectangular aperture, oriented at a position angle of 90° , was chosen to mimic the slit and east-west extraction apertures used for spectropolarimetry. The optical broad-band results for the polarization position angle are consistent with both epochs of spectropolarimetry, and also show that $\theta_R - \theta_B = 2 - 3^\circ$. The level of polarization in late 1996 is intermediate between the higher P measured in the early 1990s and the lower levels observed after 2001. We have searched the literature without finding accurate polarimetry of Mrk 231 in this interval. Thus, while it is likely that the polarization change in Mrk 231 was occurring during this period, we do not have data to determine how rapidly P varied, though the intermediate level of the data from 1996 sug-

gests that the change did not occur on very short time scales.

The effect of starlight from the host galaxy on the polarization measurements of Mrk 231 can be estimated using the imaging polarimetry. Figure 10 shows P as a function of aperture radius for both filter bandpasses. The measured polarizations at B and R for apertures ranging from $\sim 1''$ – $10''$ in diameter readily show the relative increase in starlight with aperture size. Extrapolation to $r = 0''$ of third-order polynomial fits to the measured polarization indicates that the intrinsic polarization of the nucleus is 6.45% and 3.96% in the B and R bands, respectively. The ratios of star-to-AGN light using a $10''$ aperture are 0.21 (B) and 0.64 (R). Within the typical spectroscopic extraction aperture used for spectropolarimetry ($3'' \times 10''$), the ratios are ~ 0.13 (B) and ~ 0.52 (R).

3.3. HST Imaging Polarimetry

On 1998 November 28 (UT), imaging polarimetry of the inner $\sim 1''.8 \times 1''.8$ of Mrk 231 was obtained using the Faint Object Camera (FOC) aboard the *Hubble Space Telescope* (*HST*). These observations were made in an attempt to resolve and identify the scattering regions around the nucleus. The f/96 optics of the FOC were used and the detector was read out in its smallest format (128×128 pixel) to mitigate saturation problems from the bright nucleus. To minimize the contribution of host-galaxy starlight, the observation was made in the near ultraviolet with the F346M filter ($\lambda_0 = 3480 \text{ \AA}$; $\Delta\lambda_{\text{FWHM}} = 434 \text{ \AA}$). This choice of filter also took advantage of the high polarization of the nucleus ($P \sim 15\%$ at $\lambda \sim 3000 \text{ \AA}$) measured by SSAA.

Four exposures ranging from 1166 s to 1363 s were made with each of three Polaroid filters in the beam combined with F346M. About 1.4 hr was spent using each of the POL60 and POL120 Polaroid filters, while ~ 1.5 hr total exposure time was used for POL0. In general, care must be taken with FOC polarimetry because the throughputs of the polarizer filters are not identical; however, in the F346M bandpass they are quite similar. In addition, the instrumental polarization introduced by off-axis optics inserted during the 1993 Space Shuttle *HST* servicing mission to correct the telescope's spherical aberration is not well determined (Capetti et al. 1996). Given the high polarization of Mrk 231, we have ignored the 1–3% instrumental polarization in the analysis of the FOC data since any resolved polarized regions will have even higher polarization than the $\sim 15\%$ observed in the near UV for the integrated AGN light (SSAA). The polarimetry was reduced in the manner described by Capetti et al. (1995).

The imaging data do not show any evidence for extended structure. Identification of faint extended emission very close to the point source is made especially difficult because each Polaroid filter yields a distinct point spread function (PSF). No PSF calibration images exist for the individual filter combinations, and so accurate subtraction of the PSFs is not possible. However, aperture polarimetry of the images supports the conclusion that at the resolution of the FOC, Mrk 231 is unresolved in the near UV. Circular apertures with radii of 3 pix ($0''.043$) to 33 pix ($0''.469$) all yield polarizations of

$P \approx 15.5\%$ at $\theta \approx 99^\circ$. The measurement of P is close to the value found at $\sim 3000 \text{ \AA}$ in a much larger aperture by SSAA, though the measured position angles are discrepant by nearly 10° . The difference could be caused by the instrumental polarization of the FOC. Also, the same polarization values are found for the faint emission surrounding the core of the PSF. Aperture polarimetry using an annulus with an inner radius of 6 pixels from the centroid of the bright core and an outer radius of 33 pixels also yields $P \approx 15\%$. The lack of a significant difference in the polarization between the core of the PSF and the much fainter flux surrounding the core suggests that the flux in the wings of the PSF completely dominates any resolved emission sources in the nuclear region.

The FOC data are not useful for tracking the variations in P because no other observations cover this wavelength region. What we can conclude from the near-UV imaging and polarimetry is that the nucleus and the regions scattering AGN light are small. We set a conservative upper limit for the extent of the scattering regions by using the worst of the FOC PSFs, when POL60 was in the telescope beam, with FWHM = 3.1 pixel. The data are therefore consistent with the near-UV light of the AGN (both polarized and unpolarized sources) being contained in an unresolved point source with a FWHM $\simeq 0''.044$. For Mrk 231, this corresponds to a radius of 19 pc.

Past attempts to resolve the nucleus of Mrk 231 at various wavelengths have also yielded only upper limits to the size. Ground-based near-IR and $12.5 \mu\text{m}$ observations, as well as early *HST* measurements using the Near-Infrared Camera and Multi-Object Spectrometer (NICMOS) at $1.6 \mu\text{m}$ have set limits of ~ 100 pc for the FWHM of the unresolved nucleus (Lai et al. 1998; Soifer et al. 2000; Quillen et al. 2001). Evidence for a rotating molecular torus located 30–100 pc away from central continuum source is inferred by the observations of hydroxyl maser emission (Klöckner et al. 2003). At 18 cm, Lonsdale et al. (2003) detected emission extending $0''.03$ southward of an unresolved core component with a ~ 4 pc FWHM. Recently, archival NICMOS data obtained in 1998 were re-analyzed, taking full advantage of the stable PSF of the instrument (Low et al. 2004). They set an upper limit to the diameter of the core of < 7 pc at $1.1 \mu\text{m}$. As mentioned above, the sophisticated PSF analysis employed by Low et al. (2004) cannot be used for the FOC data because of the large differences in the PSFs observed.

4. RESULTS AND DISCUSSION

4.1. X-ray Continuum and FeK α Emission

With the direct X-ray continuum of Mrk 231 blocked by a Compton-thick absorber (Braitto et al. 2004), the > 3 keV *Chandra* and *XMM-Newton* nuclear spectra are composites of indirect X-rays that reach the observer through reflection off of neutral material and/or scattering by ionized plasma into the line of sight. In this scenario, the FeK α emission is expected to be spectrally unresolved at S3 CCD resolution (FWHM ~ 200 eV at 6.4 keV). Intrinsically broad FeK α emission is generated in or near the inner accretion disk; such a line would be completely obscured by the same absorber that blocks the direct continuum. Our interpretation of the broad FeK α feature detected with *XMM-Newton* by TK as a

composite of narrow lines is more consistent with the combined *Chandra* data (with better photon statistics; see Fig. 2) as well as the physical understanding of the system. The best-fitting energies for two narrow lines fit separately in the *XMM-Newton* and combined *Chandra* spectra are 6.3 and 6.6 keV, suggesting reflection off neutral or nearly neutral material (to generate the lower energy fluorescent emission) and scattering off more highly ionized plasma (or neutral plasma with an outflow velocity of $\sim 10,000 \text{ km s}^{-1}$). This is generically consistent with the preferred model of G02 with multiple scattered lines of sight to the nucleus comprising the composite 2–8 keV spectra. However, at present the relationship between the Fe K α emission lines and the continuum emission is unclear.

A closer examination of the individual *Chandra* spectra indicates that two narrow Fe K α lines are not detected in all four observations, and therefore these features could be flux-variable on timescales of weeks. However, this is speculative at present given the photon statistics of the individual spectra.

We confirm the 2–8 keV continuum variability of $\sim 45\%$ within 6 hrs presented in G02 with a reanalysis of the *Chandra* data from observation 1031 using archival data and an updated version of the CIAO software. Variability is not detected within any of the new observations, and the overall 3–8 keV flux variability between the 4 *Chandra* observations is $\lesssim 15\%$. The difference between the 3–8 keV flux of the *XMM-Newton* observation (2001 Jun) and the combined *Chandra* observations (2003 Feb) is $\sim +20\%$ over 20 months. This is significantly larger than the measured 2–10 keV flux difference between ACIS-S3 and EPIC-pn of $\sim 5\%$ (Snowden 2001), and therefore likely indicates actual long term variability in the hard-band flux.

4.2. Na I D Absorption-Line Variations

The absorption lines involving Na I D were organized by Boksenberg et al. (1977) into redshift systems I (observed wavelength 6050 Å) and II (6015 Å), and a system at 5984 Å was added by Boroson et al. (1991). Today, the latter group is generally known as system III, though it was termed system IV as recently as Kollatschny et al. (1992).¹⁰ All three Na I D systems are apparent in the SPOL spectrum of SSAA from 1992–1993 and in our 2002–2004 spectrum (both shown at an expanded scale in Figure 9). System IIa remained approximately unchanged during the decade spanned by the observations, but the system I trough appears to have weakened slightly and system III nearly disappeared altogether. These effects are not simply a result of a difference in spectral resolution, as the spectra were obtained with the identical grating (resolution 8 Å), and other features in the same spectra, such as the narrow peak atop H α evident in Figure 9, are as apparent in the 2002–2004 data.

The rise and fall of the system III Na I D lines have been well chronicled (e.g., Kollatschny et al. 1992; FRM). The most recent characterization by Lípari et al. (2005) features a smooth decrease in line strength from a

maximum (EW = 2.2 Å) in 1988 July to EW = 0.36 Å in the data of Rupke et al. (2002) obtained in 2001 February. However, data were lacking for a 7 yr interval of the decline. Our HET UFOE spectra shown in Figure 7 were obtained near the end of the hiatus, yet neither D₁ nor D₂ were detected to an individual upper limit of EW ~ 0.03 Å, well below the detection of Rupke et al. (2002). At the same time, our spectra from the spectropolarimeter in 2002–2004 confirm their detection at approximately the same strength (Figure 9). The inference is that system III essentially disappeared altogether for a period commencing at some point after the observations of FRM in 1994 April, was absent during 2000 January and April, and reappeared weakly by early 2001. Rupke et al. (2002) also claim that the observed redshift of the feature appears to be increasing with time, though much of the historical data do not resolve the doublet.

Multi-component decomposition of the Na I D complex has been carried out under various assumptions (Rudy et al. 1985; FRM; Rupke et al. 2002), and will not be repeated here. We simply note that, apart from the absence of system III, the HET spectra closely resemble the data of Rupke et al. (2002) obtained one year later. The higher resolution of the UFOE data allows a closer examination of the narrow features near the edges of the principal system I feature. The IIc doublet, whose D₁ component lies at the blue edge of the main system I trough, has progressively increased in strength over the past decade.¹¹ In fact, the now-obvious D₂ component lies in what was a region of the continuum in the 1991 data of FRM and was only beginning to appear in their 1994 spectrum. There is marginal evidence that system IIc D₂ is slightly narrower than the system IIa features, as indicated in Table 4, however it is clear that the assignment of lines to distinct systems is meaningful only for bookkeeping purposes. There is also marginal evidence that system Ia D₁ and II D₂ are each composed of two narrow components with a separation of ~ 1 Å. We consider the identification of the II D₁ component at the blue edge of the main system I trough to be tentative, and a higher signal-to-noise ratio spectrum would be useful for separating components in this region. Finally, we point out a curious excess in the “continuum” immediately surrounding the system IIa D₁ line in Figure 7. A similar feature is apparent at somewhat lower signal-to-noise ratio in the 1994 spectrum of FRM; together the observations suggest the existence of a narrow emission component of Na I D associated with one of the absorption systems (see also FRM and Lípari et al. 1994 on this issue).

As pointed out by FRM, an interpretation of the main system I trough in terms of a few highly saturated doublets (Rudy et al. 1985) is not feasible because a column density in neutral Na as high as 10^{15} cm^{-2} develops strong damping wings, inconsistent with the observed profile. FRM’s choice of a number of optically thin components ($N_{\text{Na}} \sim 10^{13} \text{ cm}^{-2}$) over several moderately saturated doublets is based on the presence of residual flux at the bottom of the trough. However, they appear to have ignored the underlying galaxy starlight, which our imaging has shown is significant in the typical observing aperture of a ground-based telescope. The general flat-

¹⁰ The original system III of Boksenberg et al. (1977) appears only in the Balmer and Ca II H,K lines and is taken to indicate the systemic redshift of the host galaxy.

¹¹ System IIb has not been seen since the 1991 spectrum of FRM.

ness of the system I trough suggests that the individual components are optically thick, so it would seem that a blend of a number of moderately saturated lines is still an option, and the individual system column densities may well be intermediate between the above two estimates.

Starlight as the sole source of residual light in the system I trough is consistent with the lack of polarization in the bottom of the trough in 1992–1993 (Figure 9), and SSAA estimated the galactic dilution of the AGN polarization accordingly. From Figure 7, we also find that the residual flux level in the echelle spectrum of the trough, $\sim 17\%$ of the surrounding continuum level, is consistent with the host galaxy dilution expected within a $2''$ aperture. In contrast, the 2002–2004 spectropolarimetry indicates measurable polarization in the trough, with a position angle common to that of the surrounding continuum. To be sure, the net polarization in this feature is a factor of two below that of the surrounding continuum, even considering the decreased continuum polarization measured in 2002–2004. However, its presence suggests that some scattered light may have been introduced into the trough by 2002. A small amount of scattered AGN light that avoids absorption in the main system I trough would tend to support our tentative identification of the $\text{H}\alpha$ feature above.

A quantitative estimate of the intrinsic degree of polarization of the scattered light in the system I trough of Mrk 231 is strongly affected by the uncertainty in the host-galaxy contribution within the observing aperture, but it could exceed the polarization of the surrounding continuum. In high- z BAL quasars, scattered light completely dominates the residual flux in the rest-frame UV troughs, and the measured polarization can exceed 10% (Schmidt & Hines 1999; Ogle et al. 1999).

4.3. Nature of the Optical Polarization Change

The magnitude of the polarization observed in Mrk 231 and the similarity of characteristics between the emission line and continuum polarization have long been interpreted as indicating an origin in scattering (Thompson et al. 1980; Schmidt & Miller 1985). In red, strongly polarized quasars in general, and Mrk 231 in particular, there is compelling evidence in the shapes of the polarized and total flux spectra that the scattering occurs in extensive dust clouds located within ~ 100 pc of the nucleus (Goodrich & Miller 1994; SSAA; Hines et al. 2001; Smith et al. 2003, 2004). Again specific to Mrk 231, our *HST* imaging polarimetry presented above places these clouds interior to a 20 pc radius, and the fact that polarization position angle structure is observed across the $\text{H}\alpha$ emission profile (§3.2; SSAA) indicates that the broad-line region is partially resolved from the vantage point of the scattering medium, i.e., much of the scattering could occur far deeper in the nucleus. The $1.1\ \mu\text{m}$ nuclear light constrained by Low et al. (2004) to originate inside a radius of ~ 3 pc is apparently emitted by hot dust grains, the survival of which is possible as close as $\lesssim 1$ pc to a source with $L \sim 4 \times 10^{12} L_{\odot}$. In view of these facts, we imagine that *all* of the optical emission escaping from the nucleus may have undergone at least one scattering. Indeed, with optical extinction in interstellar clouds scaling as $N_{\text{H}}/A_V \sim 2 \times 10^{21} \text{ cm}^{-2} \text{ mag}^{-1}$ (e.g., Burstein & Heiles 1978), the very high absorption measured toward the X-

ray power law ($N_{\text{H}} \sim 2 \times 10^{24} \text{ cm}^{-2}$; Braitto et al. 2004) would suggest that there are no open sightlines to the central source from soft-X-ray to submillimeter wavelengths. However, as noted by Maiolino et al. (2001), the column densities from X-ray and optical extinction measures in AGN often imply much lower dust-to-gas ratios than typical interstellar clouds. Furthermore in Mrk 231, the X-ray absorber may be largely dust-free; it is likely to be much more compact than both the longer wavelength continuum emission and the dusty shroud obscuring the optical–UV continuum source.

Because scattering in a clumpy dust shroud is prone to the searchlight effect (redirection of the illuminating beam), it is not possible to relate directly the time scale for a polarization change to motion of clouds. However, the orbital period for gas at a distance of 0.5 pc from a $10^9 M_{\odot}$ black hole is 1000 yr, and so a significant change in scattering geometry over a decade is not implausible.

The following essential phenomena must be explained with regard to the observed polarization change in Mrk 231: 1) a decline in degree of polarization P , and in polarized flux $P \times F_{\lambda}$ by a factor of $\sim 1/3$ (e.g., $P_{\text{obs}} = 3\%$ to 2% at $\lambda \sim 7000 \text{ \AA}$) in both the continuum and the emission lines; 2) a position angle of polarization that has considerable structure across the spectrum but is manifestly constant with time; 3) an upper limit on the amount of any systematic change in total nuclear brightness of 15%; 4) a spectrum of polarized flux that has narrower emission lines than that in total flux; and 5) a reduction in the depth of the system I trough as well as the appearance in 2002 of significant polarization in this feature at the systemic polarization position angle.

4.3.1. The Importance of Starlight Dilution

An increase in the relative dilution by an unpolarized component is an obvious means of decreasing both the degree of polarization, P , and the polarized flux, $P \times F_{\lambda}$, without modifying the position angle. As an example, a decline in the intrinsic brightness of the AGN, while the diluting host galaxy starlight remains constant, would lead to a drop in the polarization measured within a finite aperture. The allowed magnitude of the decline is, of course, subject to our conclusion that the overall nuclear brightness varied by no more than 15% during the decade.

The lack of an aperture dependence to the polarization measurements summarized in Table 3 already argues that starlight cannot be a strong diluting component to the light measured through a typical spectropolarimetric aperture and thus is not an important factor in the polarization change. The strongest evidence for this conclusion is provided by the residual flux in the base of the system I Na I D trough, measured at 15% in 1993 and 21% in 2003 in the $3''$ aperture used with the spectropolarimeter. With stars initially accounting for no more of 15% of the total light at 6000 \AA , a change of nearly $1/3$ in polarized flux at that wavelength requires the AGN to have faded by more than a factor of four. The net spectrum in 2002 would have been far fainter than what was measured and the resulting Na I D trough would have been $<60\%$ of the continuum level.

Additional evidence of a change in polarization of the AGN component itself comes from the fact that the intrinsic (AGN-only) B -band polarization determined from

the imaging polarimetry in 1996 ($P_B = 6.45\%$, Figure 10) is no larger than the *net* (AGN + galaxy) value computed from the spectropolarimetry for the same filter passband in 1992–1993 (6.62%). Indeed, the imaging polarimetry implies that the *B*-band polarization appropriate to a $3'' \times 10''$ aperture in 1996, 5.70% (Table 3), is already well on its way to the 2002–2004 value of 5.04%.

Finally, we note that increased dilution by the opening of a new, direct (i.e., unscattered) sightline to the AGN could avoid the problem with the depth of the Na I D trough if the direct beam also passed through the system I clouds. However, this mechanism would leave the polarized flux unchanged, contrary to what is observed.

4.3.2. A Strongly Polarized Component

An important clue toward a more successful model for the polarization change was noted in §3.2: namely, the spectrum of polarized flux is not simply a reflection of the total flux spectrum. Specifically, the individual Fe II and H I emission features are much more sharply defined in the former. This is not simply a matter of contrast, but more of line width, and implies that the scattering clouds do not see the full velocity dispersion of the broad line region. The physical origin of the difference will be addressed below, but here we point out that the difference between the two spectra *requires* that a large fraction of the AGN total flux spectrum, containing the continuum, Na I D absorption, and smeared emission lines, has no polarization whatsoever. This leads to an upper limit on the amount of light that becomes polarized by scattering (because scattering is not 100% efficient at inducing polarization), and therefore to a lower limit on the degree of polarization of the scattered light.

We have carried out simple experiments to estimate the fraction of the total flux spectrum from 2002–2004 that is scattered by simply summing the spectrum of $P \times F_\lambda$ and F_λ in various relative fractions and judging by eye when the sharper features of the former are no longer visible in the total. Conservatively, we find that a higher degree of structure would be apparent in the total flux spectrum if a spectrum like that of the polarized flux comprised more than 30% of the total at a wavelength of 5500 Å. The implications are that the more sharply structured, polarized AGN component must be diluted by a virtually unpolarized AGN component (and starlight) to a ratio of at least 2.3:1, and that the intrinsic degree of polarization of the scattered light at this wavelength in 2002 was a substantial $P_{\text{sca}} \geq 3.3 \times P_{\text{obs}} = 12.5\%$! This is comparable to the observed polarization level at blue optical and near-UV wavelengths (SSAA), suggesting that the unpolarized AGN component is primarily responsible for the overall very reddened optical-UV spectral energy distribution, and that its diluting effects are greatly reduced at short wavelengths because of dust extinction. Because the polarized component is such a small fraction of the total light at visible wavelengths, a drop in the net observed polarization from 4.8% to 3.8% between the 1990’s and 2000’s at 5500 Å only requires a decline in brightness of the polarized AGN component of <30%. The change in brightness of the overall nucleus (AGN + starlight) is then <14%, consistent with the limit on the brightness change between the epochs.

4.3.3. More Complex Mechanisms

Alternate explanations for the polarization change in Mrk 231 can be constructed by the introduction of additional polarized components between the epochs. We have investigated this option by attempting to synthesize the observed flux and polarization spectra for the two epochs using the method applied by Schmidt et al. (2002) to the bipolar protoplanetary nebula surrounding CIT 6. We find that such a model can reproduce a large amount of the polarization structure seen in the Mrk 231 spectrum, and that the observed changes can be interpreted as a change in the relative brightness of the polarized components. For example, the opening of a new scattered sightline with a polarized flux spectrum like the difference spectrum shown in Figure 8, but with a polarization position angle orthogonal to the systemic angle, i.e., $\theta \sim 10^\circ$, provides an excellent match to the most recent observations. If the fractional polarization of the new sightline were large, $P \gtrsim 10\%$ at 6500 Å, the overall increase in brightness through our spectroscopic aperture would be <15%. At some level, changes in θ between epochs are also expected from this interpretation. Unfortunately, as discussed by Schmidt et al. (2002) and SSAA, even simple two-component models suffer from being non-unique, with a range of combinations of polarization, position angle, and flux level reproducing the observations with equal quality.

4.4. Dust-Reddened Quasars and the Structure of AGN

Mrk 231 can be considered the first known example of a population of optically red, IR-luminous AGN with quasar-like total energy outputs that are now being identified in significant numbers by near-IR, optical and X-ray surveys (e.g., Hines et al. 2001; Smith et al. 2002b; Matt 2002; Zakamska et al. 2005 and references therein). These objects are found in both Type 1 (broad permitted lines) and Type 2 (narrow permitted lines) varieties, and are distinguished from other samples of quasars by the fact that a sizeable fraction of each type ($\gtrsim 10\%$) show optical polarization of the total light $P \geq 3\%$, the traditional threshold for “highly” polarized AGN. Generally, the polarized Type 2 quasars have been shown to follow the basic predictions of the Unified Scheme for AGN (Antonucci 1993) by revealing broad permitted lines characteristic of a Type 1 object in polarized light. This indicates the existence of a broad line region and attests to anisotropic obscuration surrounding the central direct continuum source (e.g., Zakamska et al. 2005). The optical obscuring structure is nominally regarded as a dusty/molecular torus at $r \approx 1\text{--}100$ pc (e.g., Nenkova et al. 2002), which is seen at high inclination (i.e., edge-on) in the Type 2 systems, and the polarization is produced by scattering off particles located near the polar axis.

Though the Unified Scheme has been very effective in accounting for many key aspects of the various empirical classes of Seyfert-luminosity AGN within a single simple framework, it provides no obvious explanation for the strongly polarized Type 1 Seyfert galaxies and quasars like Mrk 231, which by virtue of the strong broad-line component in their total flux spectra are thought to be viewed at smaller inclination angles — i.e., through the “hole” of the torus. In total flux, the new population of

red quasars shows evidence for considerable reddening, whereas the polarized flux spectra are considerably bluer (Smith et al. 2003).

In an attempt to account for the $\sim 1\%$ polarization often seen in Type 1 AGNs, Goodrich & Miller (1994) and more recently Smith et al. (2002a, 2005) proposed the existence of an equatorial disk nominally coplanar with and lying inside the torus. Scattering off dust and/or electrons in this disk provides an additional polarizing mechanism for Type 1 objects. Depending on inclination angle, the observed polarization of a Type 1 AGN might be dominated by scattering off particles near the polar axis (the predominant Type 2 polarizing mechanism, for $i \sim 45^\circ$) or off the equatorial disk (for $i \lesssim 45^\circ$). The scheme of Smith et al. (2005) is currently a geometrical framework rather than a physical model, but there are clear parallels with disk-launched winds (Königl & Kartje 1994; Murray et al. 1995). If the equatorial scattering medium is identified with the disk wind, then this mechanism should not be an important source of polarization in BAL quasars such as Mrk 231.

4.5. *Toward a Model for the Nucleus of Mrk 231*

Based on the multiwavelength data available on Mrk 231, the nucleus is clearly complex with more than one structure scattering continuum and emission-line photons into the line of sight. Insight into the nucleus on the smallest physical scales in Mrk 231 is provided by X-ray observations. The most interesting constraints are provided by the combination of X-ray data from different observatories. The confirmation of Compton-thick absorption from the detection of the direct continuum at hard X-rays by Braitto et al. (2004) coupled with the continuum variability detected by G02 point towards a compact Compton-thick absorber. This opaque absorber must lie interior to the broad-line region, and therefore would not be identified with a molecular torus as are the Compton-thick absorbers in Type 2 AGNs. The X-ray absorber is likely to be on scales smaller than or comparable to the UV-optical continuum region, to enable detection of the continuum and radiative driving of the BAL outflow. As discussed in G02, the variability of indirect 2–8 keV X-rays constrains the scale of the scatterer to be $\sim 10^{15} \text{ cm}^{-2}$ and consequently the ionization of this plasma is expected to be high (i.e., with Fe almost totally stripped of electrons). The new combined *Chandra* data indicate that highly ionized plasma may have been detected in emission (with one Fe $K\alpha$ emission component at ~ 6.6 keV), though the relationship between the Fe $K\alpha$ -emitting gas and the observed 2–8 keV continuum emission is unclear. The dominant scattering mechanism in this case is electron scattering, and so this structure is distinct from the dust-enshrouded scatterer dominating the optical polarization.

On larger scales, two polarization characteristics suggest that there exists a prevailing symmetry in the unresolved active nucleus, and that some of the structures inferred by the Unified Scheme may be relevant. First, the constancy of the polarization position angle over 3 decades, despite a sizable change in P , requires that the dominant optical scattering region(s) maintain the same orientation relative to the continuum source and broad line region. Second, the individual Fe II and H I emission features are much more sharply defined in the po-

larized flux spectrum than in the total flux spectrum. The difference is better displayed in Figure 11, where we compare the total flux (less the contribution of the host galaxy; thick line) and polarized flux spectra (thin lines) for the observed-frame 5000–6000 Å region, with various amounts of gaussian smoothing applied to the polarized flux. As can be seen, the spectrum of $P \times F_\lambda$ must be convolved with a gaussian of $\text{FWHM} = 1500\text{--}2000 \text{ km s}^{-1}$ to approximate the smoothness of emission features in the total flux spectrum. Also apparent in Figure 11 is the lack of perfect correspondence between the velocity centroid of features in the two spectra, with discrepancies as large as $\sim 500 \text{ km s}^{-1}$ evident between the two. Some of these displacements are likely associated with the small polarization position angle rotations observed across the profiles of prominent emission features.

An attractive explanation for the narrower spectral features in the polarized flux spectrum is that the scattering plane is essentially orthogonal to the direction of an important dynamical motion of the line-emitting gas. Scattering off particles in polar lobes, as in the Unified Scheme for AGNs, offers such an arrangement, if the broad-line gas orbits the nucleus in a disk whose axis is nominally coincident with the lobes. The lobes also provide a natural explanation for the very large polarization inferred for this component in §3.2. The broad line region disk would also be roughly coplanar with the dust torus that presumably determines whether we perceive a Type 1 or 2 object in the total flux spectrum. Since Mrk 231 is a Type 1 AGN, the dust torus is not fully edge on, but it still serves to define the polar scattering region(s) at a position angle of $\sim 7^\circ$. The polarization properties are also consistent with an equatorial BAL outflow, though the covering fraction of the BAL wind is apparently greater than that of the torus. Furthermore, the detection of some polarized continuum unabsorbed by Na ID (Fig. 7) shows that the wind does not cover the entire sky.

The polarization position angle is closely aligned with the axis of the 40-pc scale triple source (core-lobe) imaged at GHz frequencies (Ulvestad et al. 1999a and references therein). On parsec scales, a double radio source in the nucleus is misaligned by $\sim 65^\circ$ from the larger structure (Ulvestad et al. 1999b), and therefore not coincident with the position angle of the scattering medium. Ignoring any velocity dispersion within the scattering lobes, differential projection effects across the lobes, and the unknown inclination of the orbiting disk to the line of sight, a velocity of 1500–2000 km s^{-1} corresponds to gas orbiting 1–2 pc away for a black hole at the high end of the mass distribution, $10^9 M_\odot$. Even this upper estimate for the radius is well within the upper limit to the AGN size determined by Low et al. (2004). A broad line region with dimensions of a few pc is larger than the ~ 0.3 pc estimated for objects of comparable luminosity ($\lambda L_{5100\text{\AA}} \sim 10^{45} \text{ ergs s}^{-1}$) using the reverberation technique (Kaspi et al. 2000), but the assumptions made above suggest that the velocity dispersion estimate is a lower limit, and so the disk size may be overestimated.

Smith et al. (2004) also consider the specific case of Mrk 231 and, based on the redness of the optical continuum, the presence of BAL features, and the general constancy of the polarization position angle across the

spectrum, conclude that scattering in polar lobes is the dominant polarizing mechanism. However, their assignment to “far-field” scattering in the lobes is not supported by our much higher signal-to-noise ratio data that reveal considerable position angle structure across the Balmer and Fe II emission lines, nor by the *HST* polarimetry result that locates the scattering material no further than 20 pc from the continuum source. In fact, the results of Low et al. (2004) suggest that the scattering in the polar lobes likely takes place within just a few pc of the nucleus; a much more compact scattering region than typically assumed in the Unified Scheme or actually observed in several nearby Seyfert galaxies and some quasars (see e.g., Zakamska et al. 2005) that show scattered light from regions of the order $\gtrsim 1$ kpc. However, light polarized by scattering from such a compact region would likely also be blocked by the same structure that blocks the broad-line region (with similar scales) in Type 2 objects.

The observations also require that the compact primary scattering region be enshrouded in dust to account for the lack of a narrow emission-line region. In this view of Mrk 231, the much reduced size of its polar scattering regions and the fact that light from these regions must also traverse a significant amount of dust are significant departures from the simple unified picture of AGNs. The compactness of the scattering regions and the ubiquitous dust distribution around the nucleus and possibly within the polar lobes may, in fact, be responsible for the large decrease in P observed between the early 1990s and early 2000s. One possible scenario is that dusty material interior to the main scattering clouds changed the amount of illumination within the scattering lobes or, alternatively, dust exterior to the polar lobes blocked more of the scattered light along our line of sight. In either case, large flux changes are not necessary to cause the polarization variation, and the position angle of the polarized flux will be preserved. Finally, the augmented morphology proposed by Smith et al. (2004), i.e., an additional scattering disk coplanar with the dust torus, but interior to it, may be responsible for the variation in polarization position angle across emission features and the overall rotation of θ observed throughout the optical and UV (SSAA).

4.6. Future Investigations

The holistic examination of the indirect X-ray, UV, and optical emission has provided some new insights into the nuclear structure of Mrk 231 that bear further investigation. From the close examination of the individual *Chandra* spectra, it appears that two narrow Fe K α lines are not equally strong in all four observations. A claim of flux variability between the Fe K α lines is speculative at present given the photon statistics of the individual spectra. With its higher effective area at $E > 3$ keV compared to *Chandra*, additional ~ 30 ks *XMM-Newton* observations with similar time sampling to these *Chandra* observations would be sensitive to this phenomenon.

A detection of Fe K α line variability on these time scales would constrain the location of scattering material to within the broad line region, as suggested by the continuum variability detected by G02 (and assuming the scattering media are also the sources of the Fe K α emission). A single, long-look (100–300 ks) *XMM-Newton* observation would also be productive for searching for additional hard-band variability on intermediate time scales of \sim day, for studying the iron-band features in depth, and for potentially detecting soft-band emission lines from the starburst and AGN with the Reflection Grating Spectrometer.

The lack of [O III] emission in the optical spectrum indicates that the covering fraction of dust around the nucleus is very high, thereby preventing ionizing photons from illuminating low-density gas in what would otherwise be the narrow-line region. The large-column density X-ray absorber clearly does not cover the entire sky, otherwise short-timescale variability would not be detectable. As X-rays can easily penetrate dusty gas that would block FUV photons, the X-ray narrow-line region (ionized by X-ray-energy photons) should exist and may even have already been detected (TK). In this region, the strongest features expected are the forbidden lines of O VII $\lambda 22.1$ Å and Ne IX $\lambda 13.7$ Å (e.g., Ogle et al. 2003). High-resolution X-ray spectroscopy with the next generation of X-ray observatories such as *Constellation-X* will enable a detailed emission-line study undiluted by the strong direct continuum, a rare opportunity to study the X-ray narrow-line region of a nearby, quasar-luminosity AGN.

The polarization variation we have detected in Mrk 231 is perhaps the most accurately recorded so far among radio-quiet AGN, but it is not unique. I Zw 1, which also exhibits a polarized spectrum caused by scattering, displayed a reduction in fractional amount and a rotation of $\sim 50^\circ$ in position angle between the 1980’s and 1990’s (Smith et al. 1997). Goodrich & Miller (1994) noted a 25% decline in the polarization of Mrk 509 over a 2 yr period, and a similar variation in the same object was discussed by Young et al. (1999). Smith et al. (2002a) also point out apparently significant changes in Akn 120 and NGC 7469 over periods of ~ 18 months. The fact that all are Type 1 AGNs suggests that a significant fraction of the polarization of these objects arises within the inner few pc of the nucleus, and offers hope that further studies of polarization and its variability might continue to improve our understanding of their nuclear structure.

We thank Jane Turner for generously providing reduced *XMM-Newton* spectra for comparative analysis, and Joan Wrobel and Jim Ulvestad for helpful discussions. Financial support was provided by NASA through *Chandra* grants GO3-4137 and GO3-4137B, and *HST* grant GO-6444. Support for SCG was provided by NASA through the *Spitzer* Fellowship Program, under award 1256317.

REFERENCES

- Antonucci, R. 1993, *ARA&A*, 31, 473
 Arnaud, K. A. 1996, in ASP Conf. Ser. 101: *Astronomical Data Analysis Software and Systems V*, eds. G. Jacoby & J. Barnes, vol. 5, 17
 Blandford, R. D. & Rees, M. J. 1978, in *Pittsburgh Conference on BL Lac Objects*, ed. A. M. Wolfe (University of Pittsburgh), 328–341

- Boksenberg, A., Carswell, R. F., Allen, D. A., Fosbury, R. A. E., Penston, M. V., & Sargent, W. L. W. 1977, *MNRAS*, 178, 451
- Boroson, T. A., Meyers, K. A., Morris, S. L., & Persson, S. E. 1991, *ApJ*, 370, L19
- Braitto, V., et al. 2004, *A&A*, 420, 79
- Burstein, D. & Heiles, C. 1978, *ApJ*, 225, 40
- Capetti, A., Axon, D. J., Macchetto, F., Sparks, W. B., & Boksenberg, A. 1995, *ApJ*, 446, 155
- 1996, *ApJ*, 466, 169
- Chartas, G., Gupta, V., Garmire, G., Jones, C., Falco, E. E., Shapiro, I. I., & Tavecchio, F. 2002, *ApJ*, 565, 96
- Fabbiano, G., Zezas, A., King, A. R., Ponman, T. J., Rots, A., & Schweizer, F. 2003, *ApJ*, 584, L5
- Forster, K., Rich, R. M., & McCarthy, J. K. 1995, *ApJ*, 450, 74 (FRM)
- Gabel, J. R., et al. 2003, *ApJ*, 595, 120
- Gallagher, S. C., Brandt, W. N., Chartas, G., & Garmire, G. P. 2002a, *ApJ*, 567, 37
- Gallagher, S. C., Brandt, W. N., Chartas, G., Garmire, G. P., & Sambruna, R. M. 2002b, *ApJ*, 569, 655 (G02)
- Gallagher, S. C., Brandt, W. N., Wills, B. J., Charlton, J. C., Chartas, G., & Laor, A. 2004, *ApJ*, 603, 425
- Garmire, G. P., Bautz, M. W., Ford, P. G., Nousek, J. A., & Ricker, G. R. 2003, in *X-Ray and Gamma-Ray Telescopes and Instruments for Astronomy*. Edited by Joachim E. Truemper, Harvey D. Tananbaum. *Proceedings of the SPIE*, Volume 4851, pp. 28-44 (2003), 28-44
- Gehrels, N. 1986, *ApJ*, 303, 336
- Goodrich, R. W. & Miller, J. S. 1994, *ApJ*, 434, 82
- Green, P. J., Aldcroft, T. L., Mathur, S., Wilkes, B. J., & Elvis, M. 2001, *ApJ*, 558, 109
- Hamilton, D. & Keel, W. C. 1987, *ApJ*, 321, 211
- Harlow, J. J. B., Ramsey, L. W., Andersen, D. R., Fleig, J. D., Rhoads, B. T., & Engel, L. G. 1996, *Bulletin of the American Astronomical Society*, 28, 1324
- Hines, D. C., Schmidt, G. D., Gordon, K. D., Smith, P. S., Wills, B. J., Allen, R. G., & Sitko, M. L. 2001, *ApJ*, 563, 512
- Hutchings, J. B. & Neff, S. G. 1987, *AJ*, 93, 14
- Kaspi, S., Smith, P. S., Netzer, H., Maoz, D., Jannuzi, B. T., & Giveon, U. 2000, *ApJ*, 533, 631
- Klöckner, H., Baan, W. A., & Garrett, M. A. 2003, *Nature*, 421, 821
- Kollatschny, W., Dietrich, M., & Hagen, H. 1992, *A&A*, 264, L5
- Königl, A. & Kartje, J. F. 1994, *ApJ*, 434, 446
- Lai, O., Rouan, D., Rigaut, F., Arsenault, R., & Gendron, E. 1998, *A&A*, 334, 783
- Lípari, S., Colina, L., & Macchetto, F. 1994, *ApJ*, 427, 174
- Lípari, S., Terlevich, R., Zheng, W., Garcia-Lorenzo, B., Sanches, S., & Bergmann, M. 2005, *MNRAS*, submitted, astro-ph/0501253
- Lonsdale, C. J., Lonsdale, C. J., Smith, H. E., & Diamond, P. J. 2003, *ApJ*, 592, 804
- Low, F. J., Schneider, G., & Neugebauer, G. 2004, *PASP*, in press, astro-ph/0407406
- Maiolino, R., Marconi, A., Salvati, M., Risaliti, G., Severgnini, P., Oliva, E., La Franca, F., & Vanzì, L. 2001, *A&A*, 365, 28
- Maloney, P. R. & Reynolds, C. S. 2000, *ApJ*, 545, L23
- Matt, G. 2002, *Royal Society of London Philosophical Transactions Series A*, 360, 2045
- Murray, N., Chiang, J., Grossman, S. A., & Voit, G. M. 1995, *ApJ*, 451, 498+
- Neenkova, M., Ivezić, Ž., & Elitzur, M. 2002, *ApJ*, 570, L9
- Netzer, H. & Peterson, B. M. 1997, in *ASSL Vol. 218: Astronomical Time Series*, eds. D. Maoz, A. Sternberg, & E. M. Leibowitz (Kluwer), 85
- Ogle, P. M., Cohen, M. H., Miller, J. S., Tran, H. D., Goodrich, R. W., & Martel, A. R. 1999, *ApJS*, 125, 1
- Ogle, P. M., Brookings, T., Canizares, C. R., Lee, J. C., & Marshall, H. L. 2003, *A&A*, 402, 849
- Ptak, A., Heckman, T., Levenson, N. A., Weaver, K., & Strickland, D. 2003, *ApJ*, 592, 782
- Quillen, A. C., McDonald, C., Alonso-Herrero, A., Lee, A., Shaked, S., Rieke, M. J., & Rieke, G. H. 2001, *ApJ*, 547, 129
- Ramsey, L. W., et al. 1998, in *Proc. SPIE Vol. 3352, Advanced Technology Optical/IR Telescopes VI*, ed. L. M. Stepp, 34-42
- Reeves, J. N. & Turner, M. J. L. 2000, *MNRAS*, 316, 234
- Rieke, G. H. & Low, F. J. 1972, *ApJ*, 176, L95
- Risaliti, G., Elvis, M., & Nicastro, F. 2002, *ApJ*, 571, 234
- Rudy, R. J., Stocke, J. T., & Foltz, C. B. 1985, *ApJ*, 288, 531
- Rupke, D. S., Veilleux, S., & Sanders, D. B. 2002, *ApJ*, 570, 588
- Schmidt, G. D. & Hines, D. C. 1999, *ApJ*, 512, 125
- Schmidt, G. D., Hines, D. C., & Swift, S. 2002, *ApJ*, 576, 429
- Schmidt, G. D. & Miller, J. S. 1985, *ApJ*, 290, 517
- Schmidt, G. D., Stockman, H. S., & Smith, P. S. 1992, *ApJ*, 398, L57
- Smith, J. E., Robinson, A., Alexander, D. M., Young, S., Axon, D. J., & Corbett, E. A. 2004, *MNRAS*, 350, 140
- Smith, J. E., Robinson, A., Young, S., Axon, D. J., & Corbett, E. A. 2005, *MNRAS*, 341
- Smith, J. E., Young, S., Robinson, A., Corbett, E. A., Giannuzzo, M. E., Axon, D. J., & Hough, J. H. 2002a, *MNRAS*, 335, 773
- Smith, P. S., Schmidt, G. D., Allen, R. G., & Angel, J. R. P. 1995, *ApJ*, 444, 146 (SSAA)
- Smith, P. S., Schmidt, G. D., Allen, R. G., & Hines, D. C. 1997, *ApJ*, 488, 202
- Smith, P. S., Schmidt, G. D., Hines, D. C., Cutri, R. M., & Nelson, B. O. 2002b, *ApJ*, 569, 23
- Smith, P. S., Schmidt, G. D., Hines, D. C., & Foltz, C. B. 2003, *ApJ*, 593, 676
- Snowden, S. L., 2001, in *Proc. ESTEC 'New Visions of the X-ray Universe in the XMM-Newton and Chandra Era* (astro-ph/0203311)
- Soifer, B. T., et al. 2000, *AJ*, 119, 509
- Thompson, I., Stockman, H. S., Angel, J. R. P., & Beaver, E. A. 1980, *MNRAS*, 192, 53
- Townsley, L. K., Broos, P. S., Nousek, J. A., & Garmire, G. P. 2002, *Nuclear Instruments and Methods in Physics Research A*, 486, 751
- Turner, T. J. & Kraemer, S. B. 2003, *ApJ*, 598, 916 (TK)
- Ulrich, M., Maraschi, L., & Urry, C. M. 1997, *ARA&A*, 35, 445
- Ulvestad, J. S., Wrobel, J. M., & Carilli, C. L. 1999a, *ApJ*, 516, 127
- Ulvestad, J. S., Wrobel, J. M., Roy, A. L., Wilson, A. S., Falcke, H., & Krichbaum, T. P. 1999b, *ApJ*, 517, L81
- Weisskopf, M. C., Brinkman, B., Canizares, C., Garmire, G., Murray, S., & Van Speybroeck, L. P. 2002, *PASP*, 114, 1
- Young, S., Corbett, E. A., Giannuzzo, M. E., Hough, J. H., Robinson, A., Bailey, J. A., & Axon, D. J. 1999, *MNRAS*, 303, 227
- Zakamska, N. L., et al. 2005, *AJ*, 129, 1212

TABLE 1
Chandra OBSERVING LOG

Obs. ID	Date	Exposure (ks)	Nuclear Count Rates ^a (10^{-2} ct s ⁻¹)	
			0.5–2.0 keV	2.0–8.0 keV
1031	2000 Oct 19	39.3	1.98 ± 0.07	1.92 ± 0.07
4028	2003 Feb 03	39.7	1.86 ± 0.07	1.98 ± 0.07
4029	2003 Feb 11	38.6	1.83 ± 0.07	2.00 ± 0.07
4030	2003 Feb 20	36.0	1.79 ± 0.07	2.04 ± 0.08

^aThe values are background-subtracted, though the background was negligible in the hard band and $\lesssim 3\%$ in the soft band. Nuclear source counts were extracted from a $3''$ -radius source cell. Background counts were collected from an annulus with inner and outer radii of $5''$ and $10''$, respectively, and normalized to the area of the source cell.

TABLE 2
Chandra X-RAY SPECTRAL FITTING^a

Parameter (Units)	Observation Identification					<i>XMM-Newton</i> ^b	<i>XMM-Newton</i> ^c
	1031	4028	4029	4030	4028–30		
3–8 keV Count Rate (10^{-2} s ⁻¹)	1.32±0.06	1.38±0.06	1.52±0.06	1.52±0.07	1.51±0.04
5.8–6.7 keV Count Rate (10^{-2} s ⁻¹)	0.21±0.02	0.18±0.02	0.23±0.03	0.19±0.02	0.19±0.01
F_{3-8} (10^{-13} erg cm ⁻² s ⁻¹)	4.65 ^{+0.29} _{-0.35}	4.80 ^{+0.35} _{-0.34}	5.17 ^{+0.35} _{-0.35}	5.05 ^{+0.37} _{-0.37}	5.03 ^{+0.20} _{-0.20}	4.16 ^{+0.26} _{-0.27}	4.16 ^{+0.27} _{-0.26}
L_{3-8} (10^{42} erg s ⁻¹)	1.83 ^{+0.09} _{-0.14}	1.87 ^{+0.14} _{-0.13}	2.03 ^{+0.14} _{-0.14}	1.98 ^{+0.15} _{-0.15}	1.97 ^{+0.08} _{-0.09}	1.60 ^{+0.10} _{-0.10}	1.66 ^{+0.10} _{-0.11}
Γ	0.47 ^{+0.82} _{-0.42}	0.48 ^{+0.28} _{-0.47}	0.32 ^{+0.40} _{-0.32}	0.51 ^{+0.24} _{-0.49}	0.41 ^{+0.20} _{-0.24}	0.83 ^{+0.35} _{-0.35}	0.76 ^{+0.36} _{-0.29}
Power Law Normalization (10^{-5} f _E ^d)	2.20 ^{+4.56} _{-1.10}	2.20 ^{+1.35} _{-1.01}	2.09 ^{+1.63} _{-0.80}	2.88 ^{+1.22} _{-1.53}	2.31 ^{+0.79} _{-0.68}	3.71 ^{+2.56} _{-2.20}	3.45 ^{+2.60} _{-1.27}
Line Energy (keV)	6.34 ^{+>0.66} _{->0.34}	6.68 ^{+0.08} _{-0.07}	6.34 ^{+0.04} _{-0.04}	6.4	6.31 ^{+0.08} _{-0.11} /6.64 ^{+0.05} _{-0.07}	6.47 ^{+0.13} _{-0.13}	6.31 ^{+0.11} _{-0.11} /6.62 ^{+0.10} _{-0.12}
σ (keV)	0.45 ^{+0.72} _{-0.41}	0.01	0.01	0.01	0.01/0.01	0.19 ^{+0.12} _{-0.10}	0.01/0.01
Line Flux (10^{-6} phot cm ⁻² s ⁻¹)	6.00 ^{+16.0} _{-4.7}	2.81 ^{+2.03} _{-1.70}	3.09 ^{+2.13} _{-1.62}	< 1.86	0.93 ^{+0.73} _{-0.84} /1.25 ^{+0.97} _{-0.81}	3.56 ^{+2.21} _{-1.81}	1.65 ^{+1.02} _{-1.09} /1.73 ^{+1.11} _{-1.09}
Line EW (eV)	638 ⁺¹⁷⁰⁰ ₋₄₉₉	281 ⁺²⁰⁴ ₋₁₇₀	264 ⁺¹⁸³ ₋₁₃₉	< 160	70 ⁺⁶² _{-55/98⁺⁷⁷₋₆₄}	483 ⁺²⁸³ ₋₂₇₉	143 ⁺⁸⁸ _{-95/167⁺¹⁰⁸₋₁₀₅}
Edge Energy (keV)	7.12	7.12	7.12	7.12	7.12	7.12	7.12
τ_{\max}	0.29 ^{+0.71} _{-0.29}	0.11 ^{+0.76} _{-0.11}	0.49 ^{+0.70} _{-0.49}	0.17 ^{+0.75} _{-0.17}	0.28 ^{+0.31} _{-0.27}	0.23 ^{+0.31} _{-0.23}	0.28 ^{+0.27} _{-0.28}
χ^2/ν	23.2/27	22.4/29	21.7/31	13.1/31	60.1/72	23.0/27	21.6/26
$P(\chi^2 \nu)$	0.68	0.80	0.89	0.99	0.65	0.67	0.71

^aErrors are for 90% confidence taking 1 parameter to be of interest ($\Delta\chi^2 = 2.71$). Values with no errors were fixed for the fitting. The errors for F_{3-8} , the observed-frame 3–8 keV flux, and L_{3-8} , the rest-frame 3–8 keV luminosity, were determined from 90% confidence errors in the power law normalization with all other parameters frozen to the best-fit values.

^bThe *XMM-Newton* EPIC-pn data from 3.0–10.0 keV were fit for this analysis. These spectral-fitting results are from the same data set presented in TK, and are fully consistent.

^cThe same data, fit with two unresolved Gaussians instead of a single Gaussian with σ free to vary.

^dUnits of f_E are phot cm⁻² s⁻¹ keV⁻¹.

TABLE 3
LOG OF OPTICAL AND UV OBSERVATIONS

Date (yyymmdd)	Exposure (s)	Coverage (Å)	$\Delta\lambda$ (Å)	Aperture (")	Telescope	P^a (%)	θ^a (°)
Spectropolarimetry							
First Epoch (1990's)							
19920312	800	4200–7900	17	3×10	Bok	3.36	97.5
19930226	1200	4100–7400	20	4×8	Bok	3.41	96.9
19930428	1600	4000–7300	17	3×8	Bok	3.40	96.6
19930513	4800	5630–7360	8	3×9	Bok	3.46	96.6
Mean values...						3.41 (0.04)	96.9 (0.4)
Second Epoch (2000's)							
20021204	2880	4200–8200	17	3×10	Bok	2.45	96.7
20030202	4800	4200–8200	17	3×7	Bok	2.65	98.1
20030203	2400	4200–8200	20	4×14	Bok	2.42	97.3
20030203	12800	5250–7700	8	3×13	Bok	2.33	97.0
20030307	3200	4200–8200	17	3×10	Bok	2.57	97.3
20040426	960	4200–8400	16	0.7×5	MMT	2.55	98.3
20040426	960	4200–8400	19	1.1×5	MMT	2.55	98.2
20040426	960	4200–8400	22	1.4×5	MMT	2.56	98.4
20040426	960	4200–8400	24	1.8×6	MMT	2.56	98.8
Mean values...						2.52 (0.10)	97.8 (0.7)
Imaging Polarimetry							
19961207	960	<i>B</i>	~1000	3×10	Bok	5.70	93.4
19961207	320	<i>R</i>	~1600	3×10	Bok	2.60	95.9
19981128	15520	F346M	~430	0.47	<i>HST</i>	15.3	97.8
Echelle Spectroscopy							
20000106	3×200	4534–9154	0.8	2 (fiber)	HET
20000113	4×900	4534–9154	0.8	2 (fiber)	HET
20000403	3×900	4416–8810	0.8	2 (fiber)	HET

^aFor the spectropolarimetric observations, the mean polarization properties are computed over the observed range 6100–6600 Å, a largely continuum band common to all of the datasets. For a single dataset, uncertainties are dominated by calibration, seeing, and other aperture-dependent effects as indicated by the standard deviations (in parentheses; $\Delta P \sim 0.1\%$, $\Delta\theta \sim 1^\circ$). See §3.2 for further discussion.

TABLE 4
NA I D ABSORPTION IN MRK 231

System ^a	λ_0 (Å)	λ^b (Å)	v (km s ⁻¹)	$v - v_{\text{sys}}^c$ (km s ⁻¹)	FWHM (km s ⁻¹)	EW (Å)
I	5889.950+5895.923	6047	7750	-4650	~1100	~18
Ia	5895.923	6058.82 ± 0.05	8168 ± 3	-4232	110 ± 8	0.63 ± 0.12
Ib	5889.950	6037.97 ± 0.07	7440 ± 3	-4960	101 ± 8	0.34 ± 0.11
IIa	5889.950	6013.49 ± 0.03	6222 ± 2	-6178	92 ± 6	0.54 ± 0.02
IIa	5895.923	6019.60 ± 0.03	6223 ± 2	-6177	81 ± 8	0.34 ± 0.02
IIc	5889.950	6026.81 ± 0.10	6885 ± 5	-5515	73 ± 9	0.28 ± 0.03
IIc	5895.923	6033.28 ± 0.12	6903 ± 6	-5497	48 ± 15	0.13 ± 0.04

^aThe system identifications are adopted from FRM.

^bUncertainties were estimated from Monte Carlo simulations using the noise measured in the continuum.

^cThe measured radial velocity of the line system relative to the systemic redshift of 12,400 km s⁻¹.

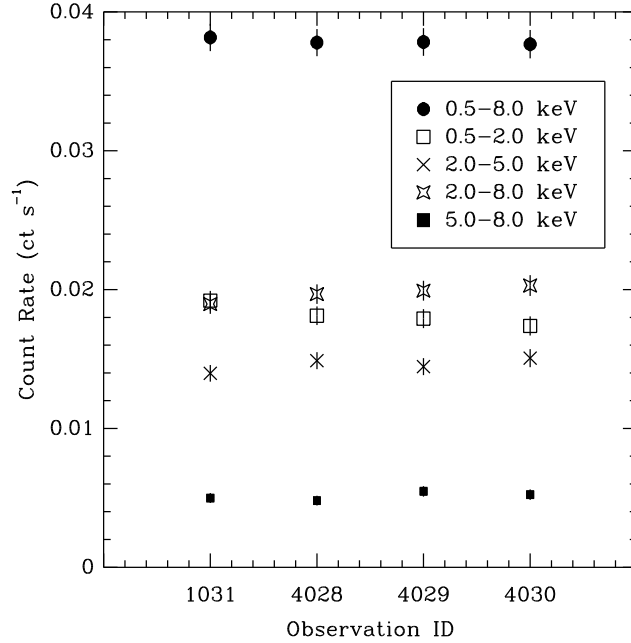


FIG. 1.— Count rates for the four different *Chandra* observations of Mrk 231. The decrease in the 0.5–2.0 keV count rate from observation 1031 to 4028 is likely a result of the declining soft-band effective area over time. Though the full-band count rate has remained remarkably stable, the slight changes in soft and hard-band count rates suggest a hardening of the spectrum.

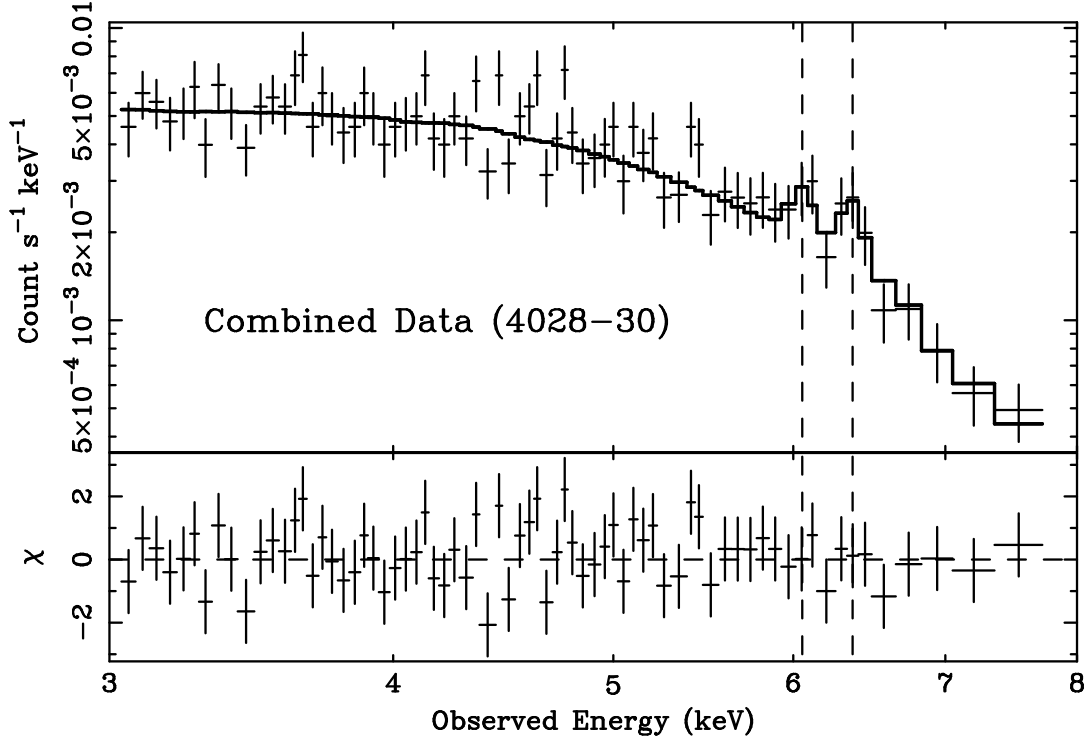


FIG. 2.— X-ray spectrum and model from the combined 3–8 keV *Chandra* data from observations 4028–30. The thick histogram is the best-fitting power-law model with two narrow gaussian emission lines and an Fe edge (see Table 2) convolved with the *Chandra* response. Vertical dashed lines mark the best-fitting energies of two narrow Fe emission lines.

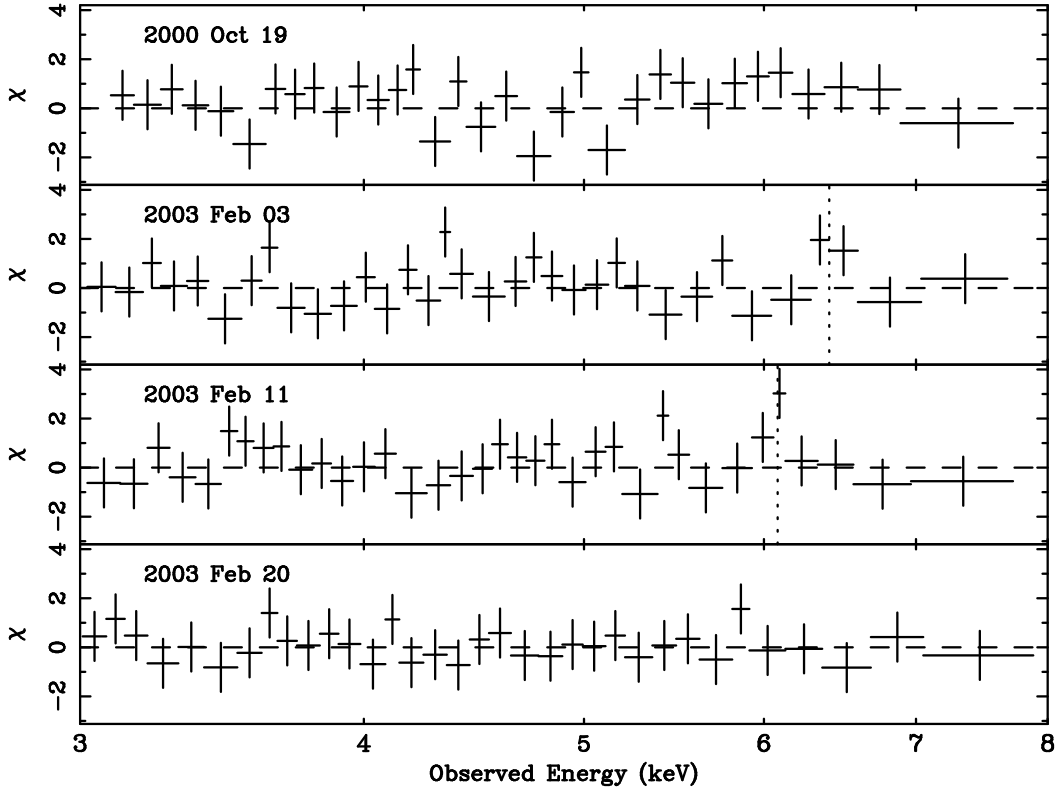


FIG. 3.— Residual plots for the four 3–8 keV Mrk 231 spectra from joint-spectral fitting. For the joint-fitting, the values of Γ and τ_{\max} were tied, power law normalizations were free to vary, and the edge energy was fixed to 7.12 keV, the energy of the neutral Fe K edge. To determine the continuum fit, the iron-band region was ignored. The energies of the two possible Fe lines are marked with vertical dotted lines.

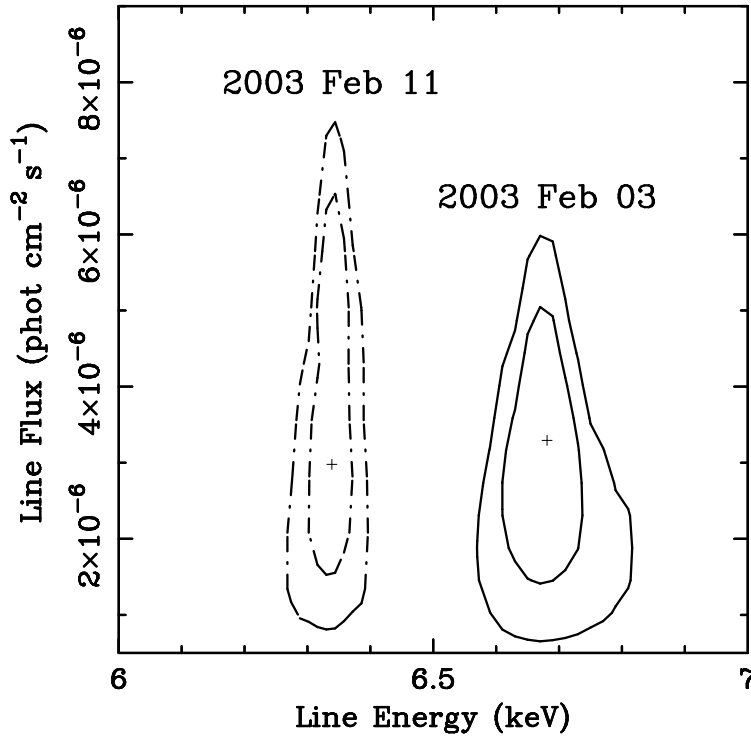


FIG. 4.— Contour plots of the line flux versus rest-frame energy of the iron lines detected in the two middle observations. The contours are 68% and 90% confidence for two parameters of interest ($\Delta\chi^2 = 2.31$ and 4.61, respectively). Though the fluxes and EWs are consistent, the energies are not.

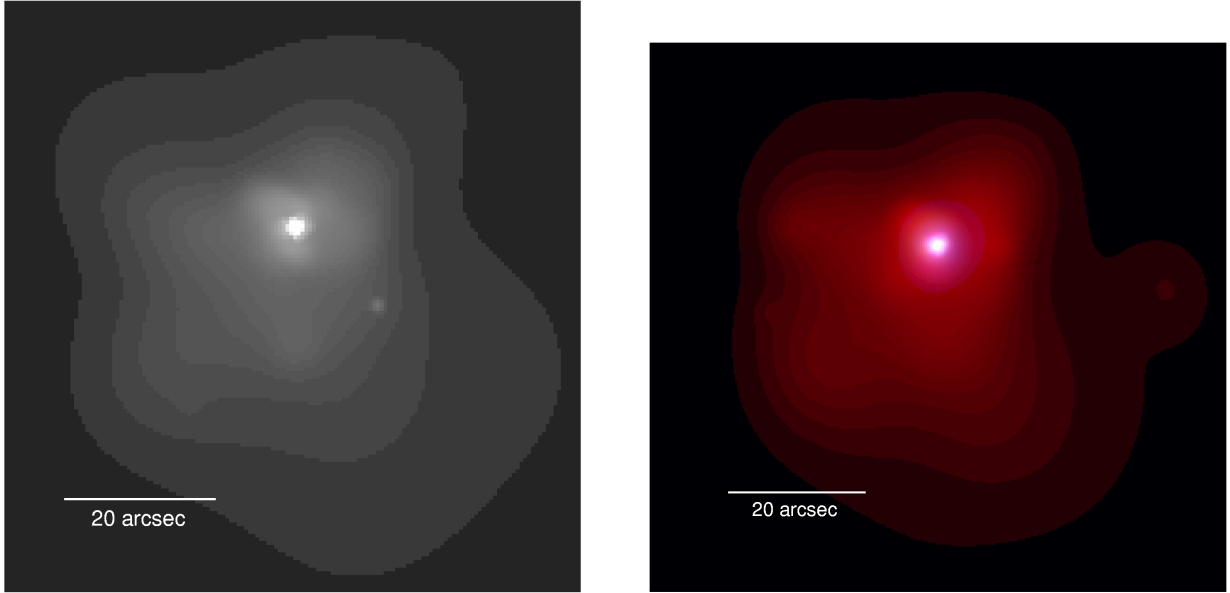


FIG. 5.— *Left panel:* Full-band, csmoothed image of Mrk 231 from the merged data sets of the three new observations. North is up and east is to the left. This 114 ks exposure reveals ring structure around the nucleus as well as a new point source to the southwest of the nucleus. *Right panel:* Three-color csmoothed image of Mrk 231 from the merged data sets of the three new observations. Red, green, and blue correspond to 0.35–1.2, 1.2–3.0, and 3.0–8.0 keV, respectively. The blue emission is slightly asymmetric, with an enhancement just to the west of the nucleus. The flat nuclear spectrum leads to the white appearance of the nucleus.

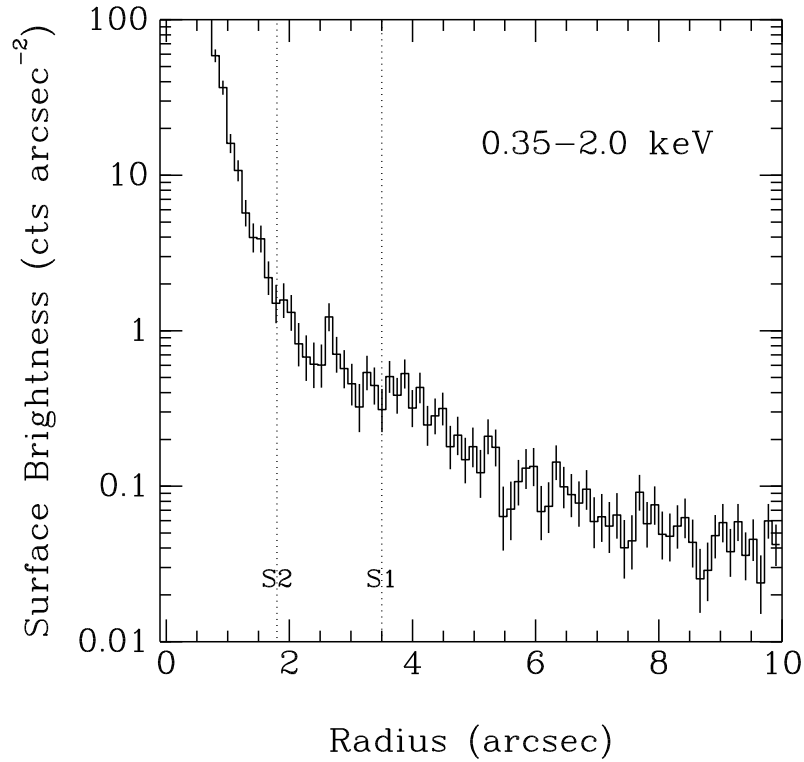


FIG. 6.— Radial surface brightness profile in the 0.35–2.0 keV band of the nucleus of Mrk 231 from the merged data of observations 4028–30. The 1σ errors have been determined using the method of Gehrels (1986). The vertical, dotted lines indicate the radii of the optical shells, S1 and S2, discussed by Lípari et al. (2005).

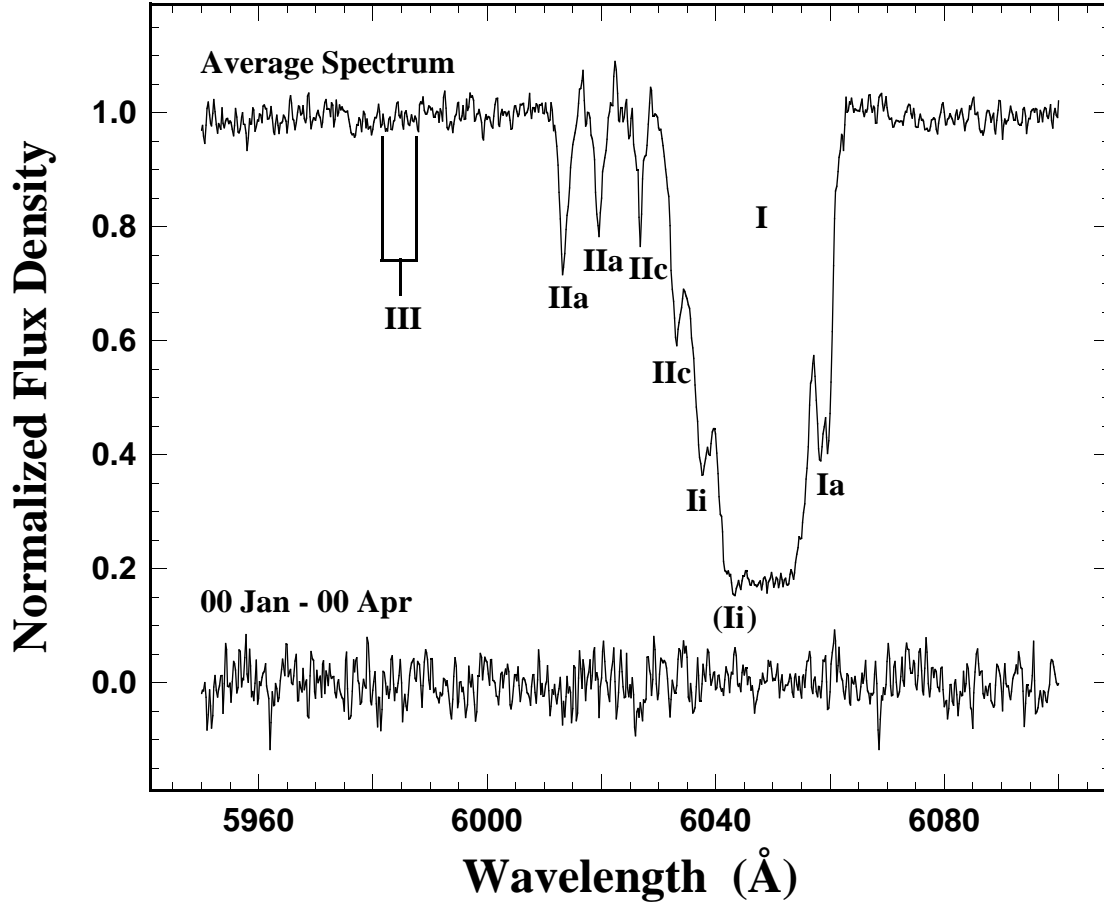


FIG. 7.— The Na I D absorption systems of Mrk 231 during 2000. The average spectrum of 2000 January and April is shown with individual line systems labeled. Systems I and II were first identified by Bokserberg et al. (1977), and are seen to break into subsystems Ia, Ii, and IIc in these much higher resolution HET echelle observations (see also FRM). The D_1 component of system Ii is tentatively identified within the main trough of system I at about the correct position relative to D_2 . Positions of the system III lines are marked, but they are not detected in these observations of early 2000. Shown below the average spectrum is the difference spectrum (Jan – Apr), which shows little evidence for change in the ~ 4 month interval.

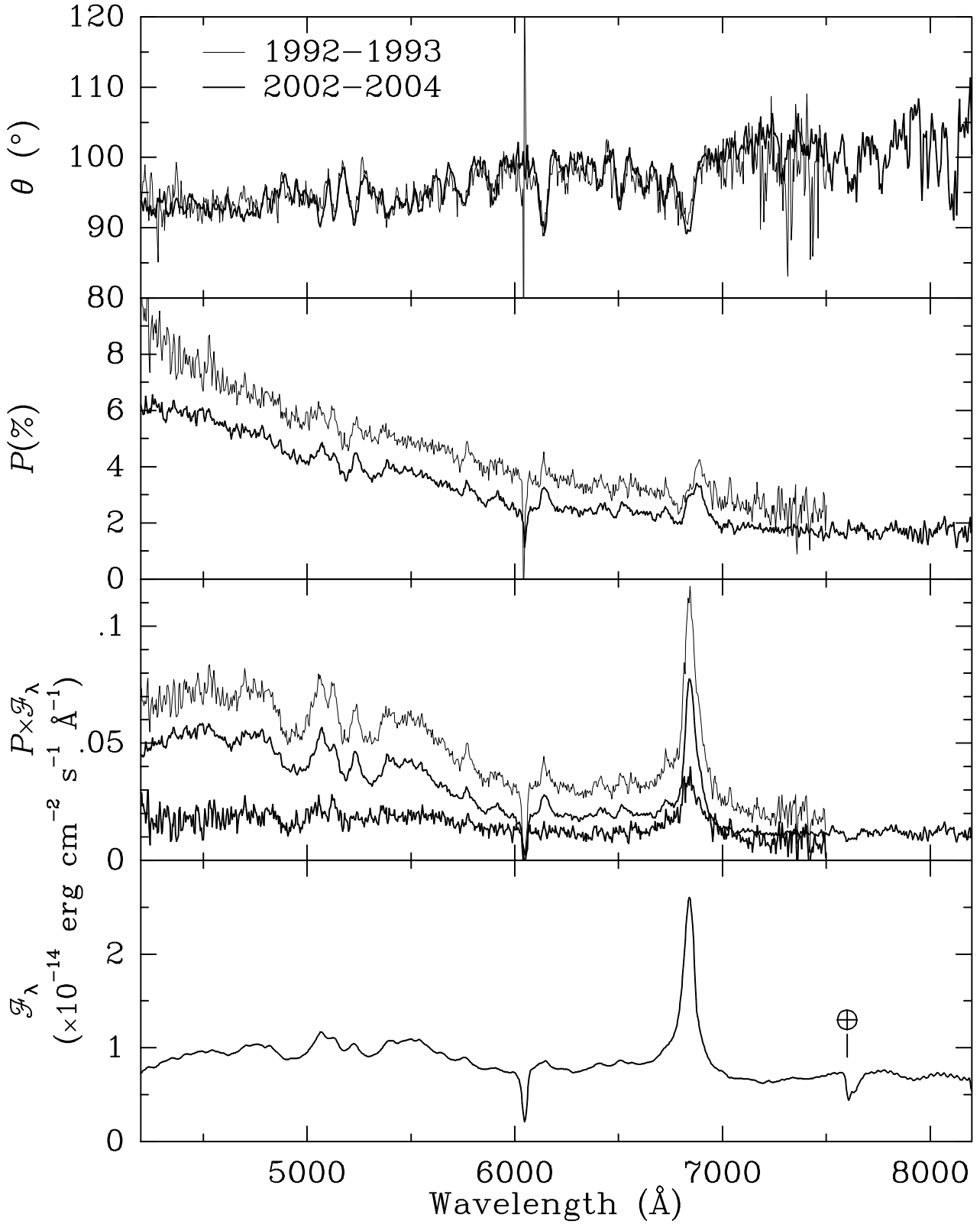


FIG. 8.— Comparison of the observed-frame, co-added polarization spectra of Mrk 231 from 2002–2004 (*thick line*) and 1992–1993 (*thin line*). Note the systematic decline by nearly 30% ($\Delta P = 1 - 2\%$ across the bandpass) in the degree of polarization with largely unchanged position angles. The polarized flux panel ($P \times F_\lambda$) also shows the difference spectrum between the two epochs (1990's minus 2000's). A representative total flux spectrum from 2003 (bottom panel) is shown for comparison. Note the much narrower profiles of the Fe II and H α emission lines in the polarized flux spectrum versus the total flux spectrum.

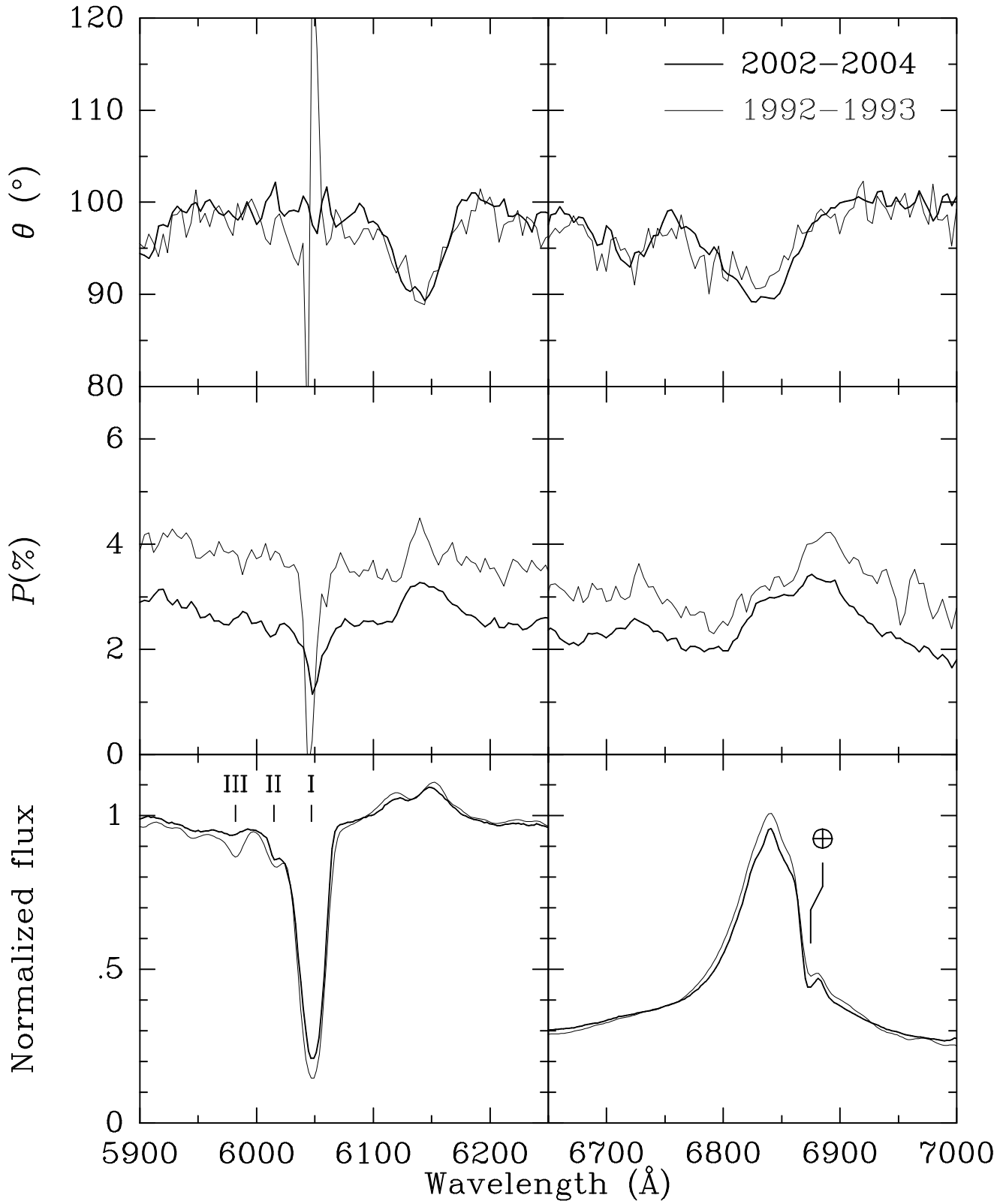


FIG. 9.— As in Figure 8 for the spectral regions surrounding the Na I D and H α lines. Roman numeral labels in the Na I D panel indicate the absorption systems described by Boksenberg et al. (1977) and Boroson et al. (1991).

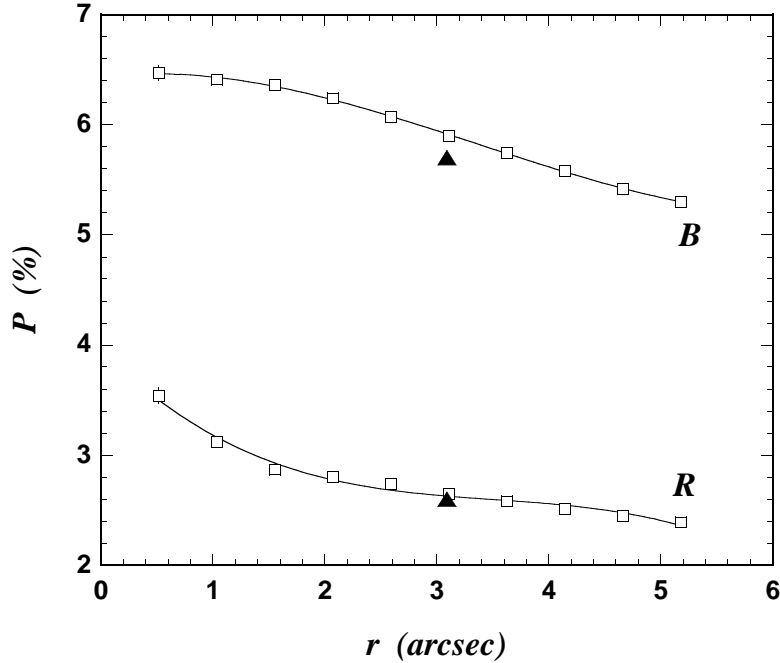


FIG. 10.— Aperture polarimetry of Mrk 231 on 1996 December 7 at *B* and *R*. In both colors there is a clear trend for P to decrease as the size of the measurement aperture is increased, indicating the inclusion of more unpolarized light from the host galaxy out to $\sim 10''$ from the unresolved AGN. *Triangles* represent the polarization with a $3'' \times 10''$, east-west aperture that approximates a typical spectropolarimetric extraction aperture used for Mrk 231.

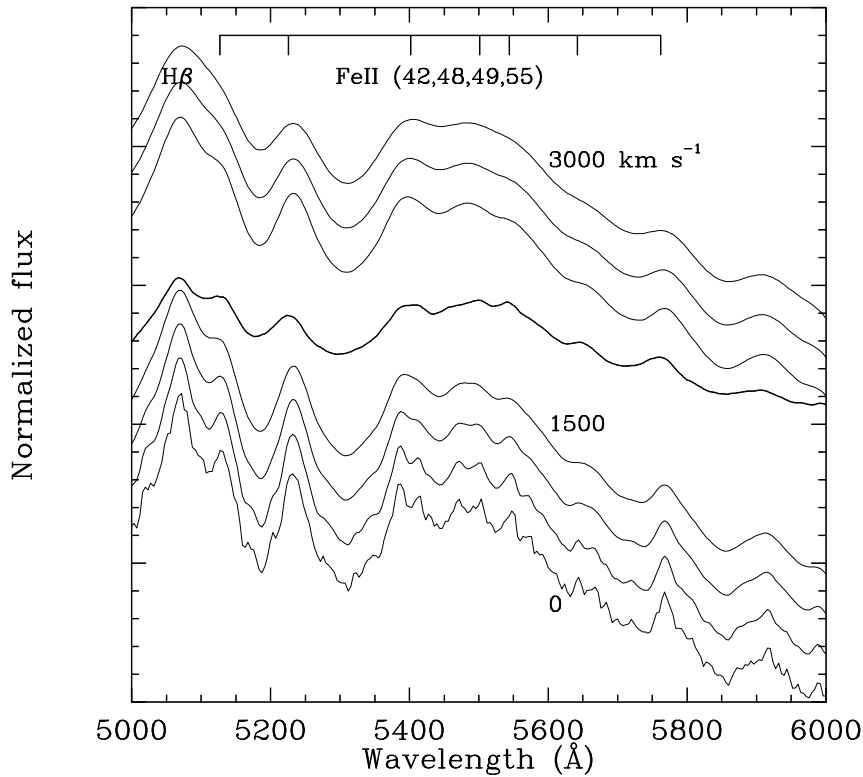


FIG. 11.— The polarized flux spectrum of Mrk 231 for 5000–6000 Å in the observed frame (thin curves) convolved with gaussians ranging from no line broadening (the observed spectrum; bottom) to FWHM = 3000 km s⁻¹ (top spectrum) in increments of 500 km s⁻¹. The thick curve is the observed total flux spectrum with the starlight contribution of the host galaxy within the observing aperture subtracted. Broadening the observed polarized flux spectrum by 1500–2000 km s⁻¹ yields an emission-line sharpness similar to that of the total light spectrum.